



Formation and vibrations of large carbon systems in the interstellar medium

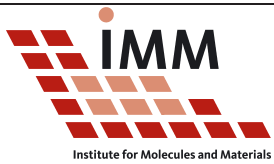
Lennert Joannes Adriaan van Tilburg

Master Thesis

May 2013

Supervisor:
Prof. dr. A. Fasolino

External adviser:
Dr. H. M. Cuppen



Theory of Condensed Matter
Institute for Molecules and Materials
Radboud University Nijmegen

Acknowledgements

This master thesis marks the end of my life as a student in physics. It was a long period in which my study had to compete for priority with many of my other interests. I was granted the opportunity to do so much more than only physics: I could learn about politics in the study association as well as in the various representative bodies in our faculty; I could organise many different activities, both topical in my field as well as with a broader scope; I could attend colloquia, symposia and conferences, I could visit companies and research institutes but also lectures on philosophy, history and culture; I could participate in the development of educational policies and teach my fellow students physics as a supervisor of exercise classes. Physics was the river that I could sail and explore the intellectual landscape along its banks.

To have these kind of opportunities is a precious thing. I am very grateful to all the people who uphold the Humboldtian academic ideal of *bildung*, the idea that an academic education is so much more than just learning about your own specific field of science. I am sad that the students who currently start their studies will not have the freedom to explore their own possibilities. Current politics have left the humanistic mindset that one should develop oneself fully and now only think of academia as a factory for producing people with specific skills who are directly useful in the economy. I do not support this notion, nor the idealisation of efficiency in academia, and I am grateful to everybody who challenges this concept, both in theory and in practise.

Finishing my master at the Theory of Condensed Matter (TCM) group was a great experience. I want to thank Jaap Kroes, Inka Locht, Leendertjan Karssemeijer en Jan Los for the use of their code. I want to thank all my roommates in HG.03.059 for their collegiality and support. Special thanks to Koen who was always in for discussions about the education policies in Holland, politics in general and, of course, religion. Merel, I want to thank you for showing me a wholesome approach for working in academia.

I want to thank my supervisor Annalisa Fasolino for all her interest in my work and beyond. I found your supervision inspiring and pleasant. You showed interest at the personal level and I felt appreciated for being myself. I had a great time at the TCM department and I learned a lot. I am also grateful to Herma Cuppen for being my external adviser. You were able to scrutinise my work on a very short notice and could point me at some fun differences in the nomenclature of physicists and chemists.

I would like to thank my parents for their continuous love and support. I am the last Van Tilburg to acquire a master's degree and I am proud be part of such a close-knid, fun and stimulating family.

Giesje, I am grateful beyond imagination for all the patience you had with me. It was sometimes quite hard to combine my life in Nijmegen with yours in Tilburg. This thesis was the last hurdle we had to tackle before we can finally live in the same place. I am looking forward to the times that come; us being together at last.

Contents

Introduction	vii
1 Carbon systems	1
1.1 Carbon allotropes	1
1.2 Crystal structure of 2 dimensional carbon	3
2 Empirical potential LCBOPII	5
2.1 Long-range Carbon Hydrogen Bond Order Potential LCBOPII	6
2.1.1 Edge reconstruction in LCBOPII	7
3 Astrophysical carbon systems	9
3.1 Fullerene formation in dense, hot plasma	10
3.2 Top-down production of fullerenes	11
3.3 Detection	12
4 Curvature	15
4.1 Continuous curvature	15
4.1.1 An intuitive approach	15
4.1.2 Mathematical refinements	16
4.2 Curvature on a lattice	17
4.2.1 Angle deficit as a measure of curvature	18
4.2.2 Ring Angle Deficit	21
4.3 Numerical evaluation of curvature	22
4.4 Temperature and curvature	22
4.5 Curvature induced by atom loss	26
4.5.1 Analysis of the curvature	28
4.6 More pentagon related curvature	29

5 Deformations and phonon Density of States	31
5.1 Theory of lattice dynamics	31
5.2 Phonon calculations with PhononLCBOP	33
5.2.1 Models of torsion	35
5.2.2 Comparison of DOS to single configurations	38
5.2.3 Finite samples and finite temperature	40
5.2.4 Imaginary modes	41
5.2.5 Comparison of the calculated DOS with experiment	47
5.2.6 Temperature effects of the phonon Density of States	48
5.3 The phonon spectrum and structural differences	49
5.3.1 Variations in carbon configuration	49
5.3.2 Edge termination differences	52
5.3.3 Defects in the lattice	52
5.3.4 Effects of curvature on the DOS	55
6 Summary and discussion	57
A List of stuctures	59
Bibliography	61

Introduction

Carbon; this thesis is about carbon. For most people this material is one of the most mundane substances used for instance in pencils and filtration systems. However, to scientists this element has a richness in theoretical depth and applicability beyond imagination. In all fields of natural science, carbon is of high importance. It forms the backbone of all organic compounds with, at its pinnacle, the DNA molecule, the basis of life as we know it. In physics, carbon has only just begun to show its full potential. It is not a coincidence that the Nobel Prize for Physics in 2010 was awarded to Geim and Novoselov [9] for their research on the properties of graphene, the perfect two-dimensional carbon. Graphene is a model system for describing the properties of membranes [15] and for studying relativistic quantum effects [17]. In astrophysics carbon systems are studied to understand how organic molecules form in space, a field of science called astrobiology. The abundance of carbon in many forms, graphene flakes, graphite, diamond and fullerenes gives us information about stellar evolution, interstellar dynamics and astrophysical carbon chemistry.

The inspiration for the work presented in this thesis lies in this scope. Recent observations of fullerene abundances in (interstellar) space motivated the study of the formation pathway for carbon allotropes. Instead of the aggregation of small carbon clusters into closed systems, large flat polycyclic aromatic hydrocarbons fold up under intense radiation. Carbon loss induces curvature and thus bends the flake into closed structures. These ideas were presented by Olivier Berné [2] at the weekly group seminar of the Theory of Condensed Matter group at the Radboud University Nijmegen and inspired me and my supervisor Prof. Annalisa Fasolino to study some aspects of the proposed mechanism.

“Yes, we too are stardust.”

—Major Albert Knag to Hilde in Jostein Gaarder’s Sophie’s World. [8]

The thesis is divided in the following parts:

In **Chapter 1** we introduce the basis carbon physics and the two dimensional graphene.

In **Chapter 2** we explain the computational method used in the research presented in this thesis.

In **Chapter 3** we present the two pathways in fullerene production in space. We also describe the detection of these fullerenes by infrared spectroscopy.

In **Chapter 4** we develop two methods to describe curvature on a lattice and use them to describe the dependence of curvature on temperature. We also show the way our measure for curvature enables us to study the atom loss induced curvature in detail.

In **Chapter 5** we explain the theory of lattice dynamics and use phonon density of states to characterise defected and curved carbon systems.

In the **appendix** we list the studied systems for quick reference.

Chapter 1

Carbon systems

Carbon is a very versatile element. In this chapter we will review some manifestations of carbon, discuss the way it chemically bonds and describe the crystal structure of the two dimensional carbon system graphene.

1.1 Carbon allotropes

Carbon has many (meta)-stable forms in which it can exist, called allotropes. The way these allotropes are structured has a profound effect on the properties of the material. We label them by their “dimension” although it must be noted that they are of course embedded in three dimensional space. The two most commonly known configurations are diamond and graphite. The first is renowned for its hardness and brilliance; the second is used by everybody in pencils but has also applications as a lubricant and in electrodes. Although graphite is the most stable allotrope under ambient conditions, the reaction pathway from diamond to graphite is suppressed by a large energy barrier (0.33 eV per atom) [7].

Graphite consists of stacked layers of the 2D manifestation of carbon: graphene. This substance was first created by Novoselov and Geim [28]. Since then, the study of this material has been one of the major subjects of enquiry in material science and its discovery was rewarded with the Nobel Prize in physics in 2010. When a graphene sheet is folded onto itself, a nanotube is formed. These cylinder-like structures can have a ratio between length and diameter of several orders of magnitude and can therefore be described as one dimensional. The zero dimensional fullerene (or buckyball) finishes the list. Figure 1.1 shows the mentioned arrangements of carbon.

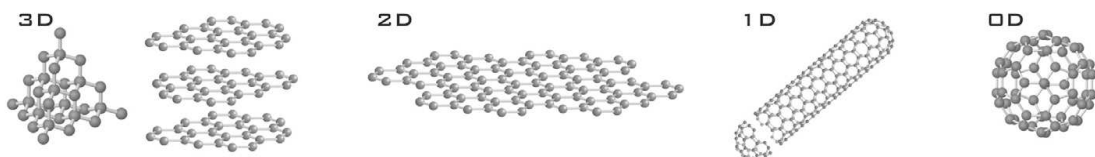


Figure 1.1: Allotropes of carbon. From left to right: 3D diamond & graphite; 2D graphene, 1D nanotube and the 0D fullerene. Picture from [16].

Carbon can also form in an amorphous state with only short-range order. This is the case in charcoal and soot. The rich spectrum of stable carbon arrangements leads to very distinct physical properties. Where diamond is hard, layers of graphite can easily be separated from each other. The conductivity of both heat and electricity also greatly varies between diamond and (within) the graphitic systems. The reason for this lies in the nature of the chemical bonds of the atoms in the lattice. Carbon atoms have six electrons. The electrons are arranged in shells where the total number of electrons that can fit in shell n is $2n^2$. For carbon, the first two electrons thus reside in the first shell, the $1s$ orbital which is then filled. The second shell has both an s orbital and a p orbital. The former can fit another two electrons and the latter another six. Since electrons repel due to coulomb interactions, the p electrons will occupy different suborbitals to increase spatial separation. The electronic ground state of atomic carbon can be written down as $1s^2 2s^2 2p^2$.

However, when carbon is close to other atoms it can rearrange its electron configuration. One of the $2s$ electrons is excited to the empty p suborbital. This costs some energy since the angular momentum of the system gets larger, but it also increases binding energy of the p electrons because the screening of the nucleus is reduced. The electrons rearrange and the resulting orbitals are a linear combination of the $2s$ electron and (some) of the p orbitals. We speak of hybridised orbitals; depending on the number of p orbitals that are mixed we have sp , sp^2 and sp^3 hybrid orbitals. Each alternative has a different spacial structure, shown in figure 1.2. The sp^2 orbitals make three equivalent planar bonds. To minimise coulomb repulsion these bonds have angles of 120° . The remaining p electron is in an out of plane orbital. These orbitals aid in interplanar bonds between different layers of carbon like in graphene.

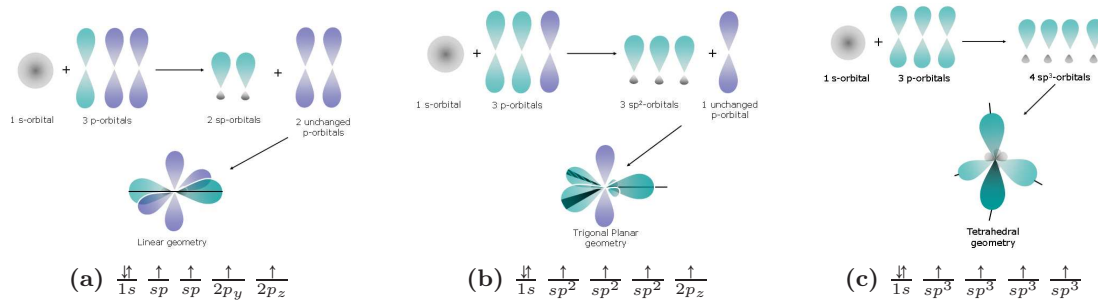


Figure 1.2: Electron rearrangement to form hybrid bonds, (a) sp : two linear hybrid orbitals, (b) sp^2 : three planar hybrid orbitals at 120° , (c) sp^3 : four hybrid orbitals at 109.5° . Geometry and electron distribution in the orbitals is shown. Pictures from [32].

The hybrid orbitals form very strong and stable bonds, making carbon a very good “building block” for many substances. It bonds easily and in many different ways. Silicon, the element directly under carbon in the periodic table, shares the same electronic configuration but is less willing to combine in all these ways. This can be explained by the small mass of carbon. As one of the lightest elements it has very closely spaced orbitals than can easily combine. A good example is the benzene molecule C_6H_6 where the carbon atoms are sp^2 hybridised. The six remaining p_z orbitals are so close together that they are shared by all carbon atoms (creating delocalised states), a process called conjugation.

1.2 Crystal structure of 2 dimensional carbon

As mentioned before, the sp^2 hybridisation of the carbon orbitals creates three planar bonds with 120° angles. The 2D carbon system graphene thus forms a honeycomb lattice. The atoms are separated by a distance $a \approx 1.42 \text{ \AA}$. The honeycomb lattice is not a Bravais lattice but is built up from two triangular sublattices (A & B) with separation

$$\delta = a \begin{pmatrix} 1 \\ 0 \end{pmatrix}.$$

These are shown in figure 1.3 as filled and open circles. Graphene thus has a triangular lattice with two atoms per unit cell. The unit cell has the following lattice vectors:

$$\mathbf{a}_1 = a \begin{pmatrix} \sqrt{3} \\ 0 \end{pmatrix}, \quad \mathbf{a}_2 = \frac{1}{2} a \begin{pmatrix} \sqrt{3} \\ 3 \end{pmatrix}. \quad (1.1)$$

The corresponding reciprocal lattice vectors are defined by $\mathbf{a}_i \cdot \mathbf{b}_j = 2\pi\delta_{ij}$, with δ_{ij} the Kronecker delta which is one if $i = j$ and zero otherwise. This gives us

$$\mathbf{b}_1 = \frac{2\pi}{a} \begin{pmatrix} \frac{1}{\sqrt{3}} \\ -\frac{1}{3} \end{pmatrix}, \quad \mathbf{b}_2 = \frac{2\pi}{a} \begin{pmatrix} 0 \\ \frac{2}{3} \end{pmatrix}. \quad (1.2)$$

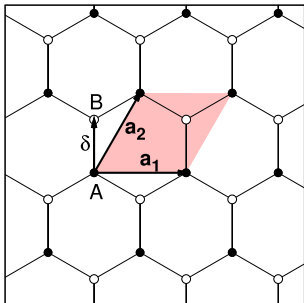


Figure 1.3: The two triangular sublattices A (filled circles) & B (open circles) in real space and the connecting vector δ . The basis vectors \mathbf{a}_1 and \mathbf{a}_2 for the lattices are shown. The shaded area is the unit cell which contains two atoms. Picture based on figure 1.3 from [14].

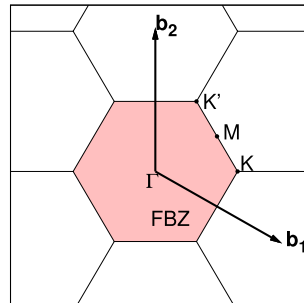


Figure 1.4: Basis vectors for the reciprocal lattice. The shaded area is the first Brillouin zone. The sides of the zone have length $\frac{2\pi}{a} \frac{\sqrt{3}}{3}$. Points of high symmetry are indicated. Picture from [14].

The first Brillouin zone of the triangular lattice is a regular hexagonal cell, shown in figure 1.4. The first zone has a number of points with special symmetry. The Γ point ($\mathbf{q} = 0$) captures the translational symmetry of the structure, points \mathbf{K} and \mathbf{K}' are at the zone edge. Here the conduction band and valence band meet. Point \mathbf{M} lies halfway between the corners of the Brillouin zone. These points are very useful for computing the phonon dispersion of graphene and we will see them again in chapter 5.

Chapter 2

Empirical potential LCBOPII

The structures described in the previous chapter can be studied in various ways. Experimental methods give us valuable insight in parameters of the systems under investigation. They can provide a phenomenological framework in which we can describe the physical patterns that we see. Theoretical work shows us how bare theory describes systems in detail. Both approaches have their advantages and drawbacks. A computational technique stands in between and can provide a bridge between experiment and theory. By means of simulations one is able to acquire the results of very complicated calculations for fairly large systems, both in experimental conditions and beyond. This chapter introduces the numerical method used for the computational work presented in this thesis.

Atomistic simulations

If one wants to calculate the properties of a complex system there are two pathways. The first is a calculation from first principles (also called *ab initio*) that solves Schrödinger equation. Examples are Density Functional Theory and Hartree-Fock methods. They are, however, computationally costly since, for a many body problem, the number of variables is large. The second approach in constructing computational techniques uses empirical potentials. Such a potential models the interaction between particles by only a few parameters. Subsequent terms in the potential describe the underlying physics of a system. The value of the parameters of the potential are fitted to results of experiment and theory. This greatly reduces the computational time and needed resources and thus makes it possible to study larger systems a lot faster than in *ab initio* simulations.

The two most important simulation schemes that use often an empirical potential are Molecular Dynamics (MD), an algorithm based on solving (classical) equations of motion and Monte Carlo (MC), based on the gathering of statistical averages via (selective) sampling of the phase space. Although MD uses classical laws of motion, this is only a setback when dealing with the lightest elements. For heavier particles (like carbon) the electronic part of the system evolves much faster than the positions of the nuclei. If the potential also includes quantum mechanical effects it will give proper results. In MC, the method of selecting points in phase space where physical parameters are evaluated, is key to the effectiveness of the simulation. Since every state is weighed by its Boltzmann factor, an efficient way of selecting which state to sample can greatly influence the performance of the simulation. An example of such a selection scheme is the *Metropolis algorithm* [27]. Under the right numerical conditions the MD and MC simulations can be viewed as a path in the phase space of the microcanonical (NVE) and the canonical ensemble (NVT) respectively.

2.1 Long-range Carbon Hydrogen Bond Order Potential LCBOPII

The main computational tool used in the work presented in this thesis is the bond order potential LCBOPII. Developed by Los and Fasolino [22] in 2003, it was able to correctly describe the short range covalent bonds between carbon atoms and also to get correct values for the inter planar bonding between graphitic layers. The potential was subsequently improved [23] & [10] to accommodate for torsion and medium range interaction terms, used to describe breaking and forming of bonds. The latter improves the reactive properties of the potential.

The LCBOPII empirical potential uses the following expression to calculate the total energy of a certain configuration of atoms:

$$E_{tot} = \frac{1}{2} \sum_{i,j}^N \left(S_{ij}^{sr} V_{ij}^{sr} + S_{ij}^{lr} V_{ij}^{lr} + \frac{1}{Z_i^{mr}} S_{ij}^{mr} V_{ij}^{mr} \right). \quad (2.1)$$

In this formula, ij sums over all pairs of N atoms and V takes a value for the three different ranges of the potential. Switch functions S_{ij} provide a smooth connection between the three interaction ranges. LCBOPII is a pair interaction potential that depends mostly on the interatomic distance c.q. $V_{ij} = V(\mathbf{r}_{ij})$, $S_{ij} = S(\mathbf{r}_{ij})$ with \mathbf{r}_{ij} the distance between atom i and atom j : $\mathbf{r}_{ij} = |\mathbf{r}_i - \mathbf{r}_j|$. The short-range and long-range interaction meet at $1.7 \leq \mathbf{r}_{ij} \leq 2.2$; here the switch functions provide a transition: $S^{lr} = 1 - S^{sr}$. Figure 2.1 shows the range of all interactions whereas the resulting potential for a certain environmental configuration is shown in figure 2.2.

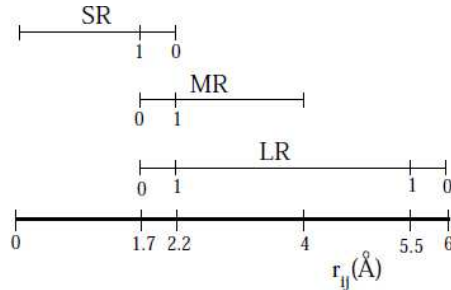


Figure 2.1: Range of the three interaction terms (short-range: SR, medium-range: MR and long-range: LR) in LCBOPII. The numbers 0 and 1 depict the location where the interaction is smoothly turned on or off. The SR and the LR connect at 1.7 to 2.2 Å. Picture from Ghiringhelli et al. [11].

The long-range part of LCBOPII is a Morse-like potential that is tuned to produce correct results for the interlayer binding in graphite sheets. The short range mainly deals with nearest neighbour interactions. It is a modified Brenner type [3] interaction with a repulsive part V_R^{sr} and an attractive part V_A^{sr} that combine to

$$V^{sr}(\mathbf{r}_{ij}) = V_R^{sr}(\mathbf{r}_{ij}) - B_{ij} V_A^{sr}(\mathbf{r}_{ij}). \quad (2.2)$$

The term B_{ij} is the *bond order*. It is a measure for how the bond between atom i and j is built up. It includes many body effects such as conjugation, angular dependencies and coordination.

The last part of formula 2.1 is the middle-range term. The factor Z_i^{mr} acts as a coordination number for medium range effects. It is sensitive to the presence of dangling bonds and other environmental parameters.

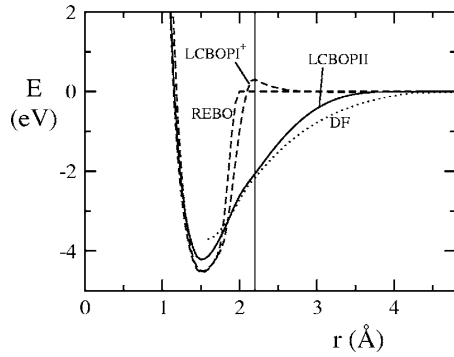


Figure 2.2: Bonding energy for the single bond in $(\text{CH}_3)_3\text{C} - \text{C}(\text{CH}_3)_3$ as a function of the central C – C distance. The dotted line (DF) shows *ab initio* results. The solid line is the potential of LCBOPII. Two other empirical potentials are shown. There is a good correspondence between DF and LCBOPII in the medium range ($1.7 \leq r \leq 4.0$). Picture from Los et al. [23].

Its switch function S^{mr} is chosen in such a way that it does not influence the equilibrium properties of the bulk phases but is restricted to effects that involve the making and breaking of bonds. It makes the potential more reactive and therefore useful in describing transitions in structure such as defects [23] and melting [36].

2.1.1 Edge reconstruction in LCBOPII

Adding the middle range term was a big improvement as shown in figure 2.2. Another improvement by Kroes et al. [20] included an edge reconstruction term. As predicted by Koskinen et al. [18], at the edge of a graphene ribbon the *armchair* (AC) configuration has a lower energy than the *zigzag* (zz) configuration. This has to do with the fact that in the AC situation, one of the outer C-C pairs almost forms a triple bond. If the energy barrier of 0.83 eV is overcome, a zz edge can locally reconstruct to a configuration called zz(57), resembling the AC structure. Figure 2.3 shows the three configurations and the bond lengths at the edge. Including the reconstruction term in the potential has profound effects on aggregation results of a carbon gas, as we will see in chapter 3, and on the calculation of the phonon spectrum of a flake, explained in chapter 5.

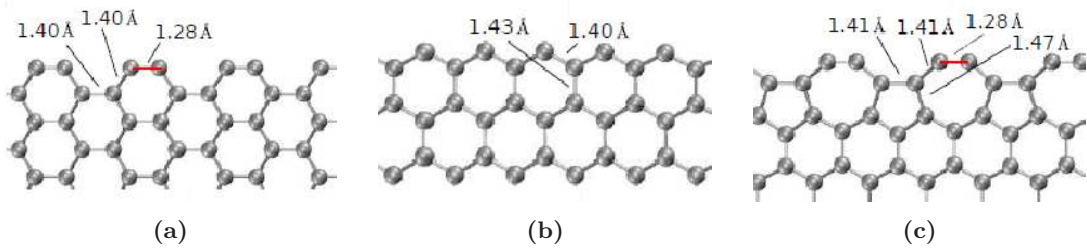


Figure 2.3: Edge configurations of graphene and equilibrium interatomic distances for the edge atoms. (a): armchair AC, (b): zigzag zz, (c): reconstructed zz(57). In red, the enhanced bond is shown. Picture based on figure 1 from Kroes et al. [20].

Chapter 3

Astrophysical carbon systems: formation and detection

Atomic carbon is formed by fusion in stars. It is produced in the triple-alpha process where three Helium nuclei fuse to an excited state of carbon-12 via an intermediate Beryllium nucleus. The carbon that is formed can get expelled from the system via various astrophysical phenomena. It is recently discovered that atomic carbon can cluster into more complex structures, including the fullerenes C₆₀ and C₇₀, see figure 3.1. These are hitherto the largest molecules found in space that can be uniquely identified. The formation process of these fullerenes is an active research topic in interstellar organic chemistry since it can provide an insight in early carbon chemistry in space.

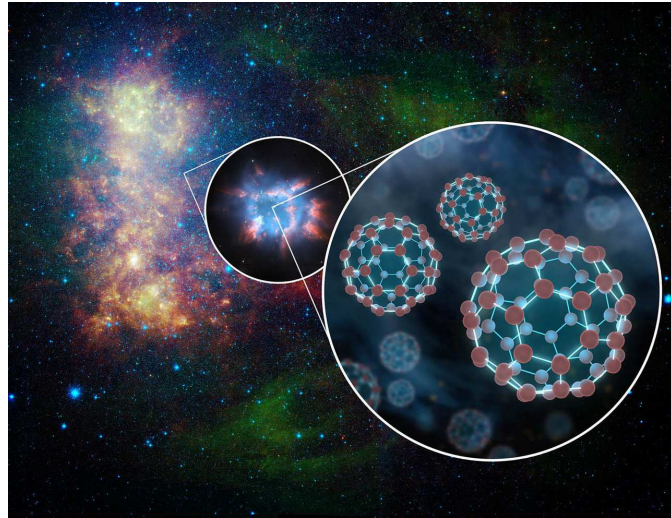


Figure 3.1: Superimposed on a Spitzer space telescope infrared photo of the Small Magellanic Cloud is an artist's illustration depicting a magnified view of a planetary nebula and an even further magnified view of the found fullerenes. Picture from [31].

3.1 Fullerene formation in dense, hot plasma: the bottom-up route

Depending on the environment of the carbon, there are two proposed pathways in the formation of the fullerenes. In the hot and dense ($T > 1500$ K, $n > 10^{11}$ cm $^{-3}$) envelopes of evolved stars (stars that have fully burned their hydrogen) carbon is abundant enough to aggregate into chains and rings that later fuse to form fullerenes. This is the so called *bottom-up* route and was explained by Heath [13], Goroff [12] and Cherchneff et al. [5]. We have performed a qualitative study of the aggregation process by putting 400 carbon atoms in a $70 \times 70 \times 70$ Å 3 box with periodic boundary conditions. The initial positions of the atoms were randomly chosen on an imaginary cubic lattice with basic vectors of length 5.0 Å. We performed a MC simulation in the canonical ensemble at 2000 Kelvin. Figure 3.2 shows two stable configurations that were formed in the aggregation process. In the simulation resulting in the left figure, the edge reconstruction, explained in section 2.1.1, term was switched off whereas the right figure was produced in a simulation that included the algorithm.

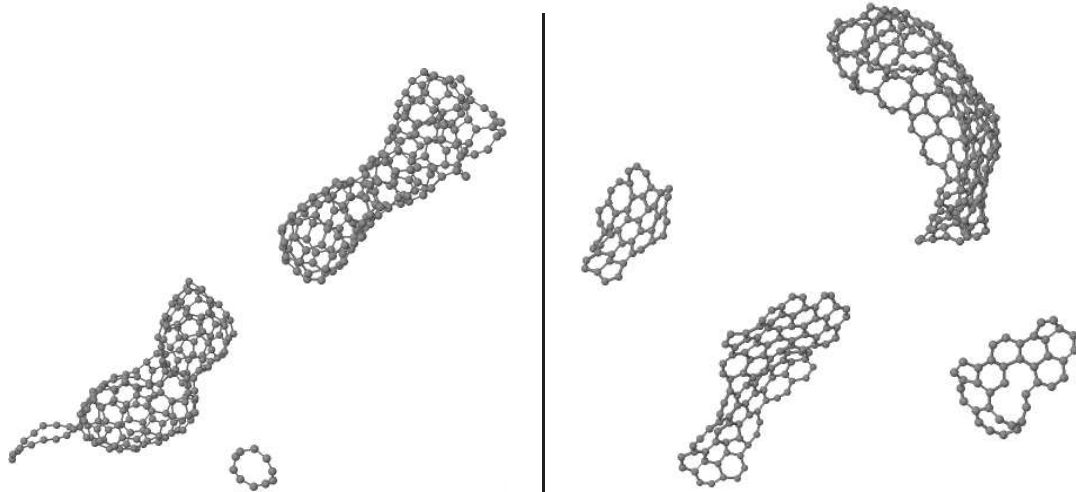


Figure 3.2: Typical configurations after many MC steps for an aggregation simulation at 2000 Kelvin. The carbon gas has clustered into compact forms. The final result is different for simulations that do not take the edge reconstruction term in the potential into account (left) and those that do (right).

Both simulations show similar behaviour at the start. The carbon atoms fuse into chains that later on form rings. These small clusters merge and the typical hexagonal lattice becomes visible. In the simulations that included the edge algorithm the clusters grew but did not close into carbon cages whereas that did happen in the simulations where the algorithm was switched off. Although the structure in the top right corner of figure 3.2 has a bowl-like configuration, it does not bend further to close.

It is clear that the edge algorithm has a profound effect on the aggregation result. This has two main reasons. Firstly, the algorithm penalises out of plane bending of the edge because it enhances the tensile stress in the edge [20]. Secondly; because it makes the bonds at the edge stronger, it also limits the edge reactivity. This hinders the formation of caged structures since edges that meet do not easily connect. In the simulations without the edge reconstruction algorithm this *does* happen, closing the flake. This process is called “zipping” and is very important in explaining how curvature of carbon flakes leads to fullerenes.

3.2 Top-down production of fullerenes

Recent observations with the *Spitzer* space telescope [34] showed the existence of the fullerenes C₆₀ and C₇₀ in the interstellar medium (ISM) [30]. These regions of space are cold and tenuous so it is not likely that closed structures are formed by aggregation of atomic carbon. Another model was proposed to explain the observation. Berné and Tielens [2] introduced a top-down formation pathway in which carbonaceous compounds isomerise to fullerenes. The compounds themselves are formed in the aggregation process described in the previous section. After their ejection into the ISM they are saturated with hydrogenation. They mostly form Polycyclic Aromatic Hydrocarbons (PAH), flat graphene flakes terminated by hydrogen. If these PAH's end up near a bright ultraviolet radiation star, they are converted into graphene flakes by photodissociation. Subsequent carbon loss produces pentagons that induce local curvature. The flakes curl up and form fullerenes. Figure 3.3 shows the general scheme for this *top-down* fullerene production.

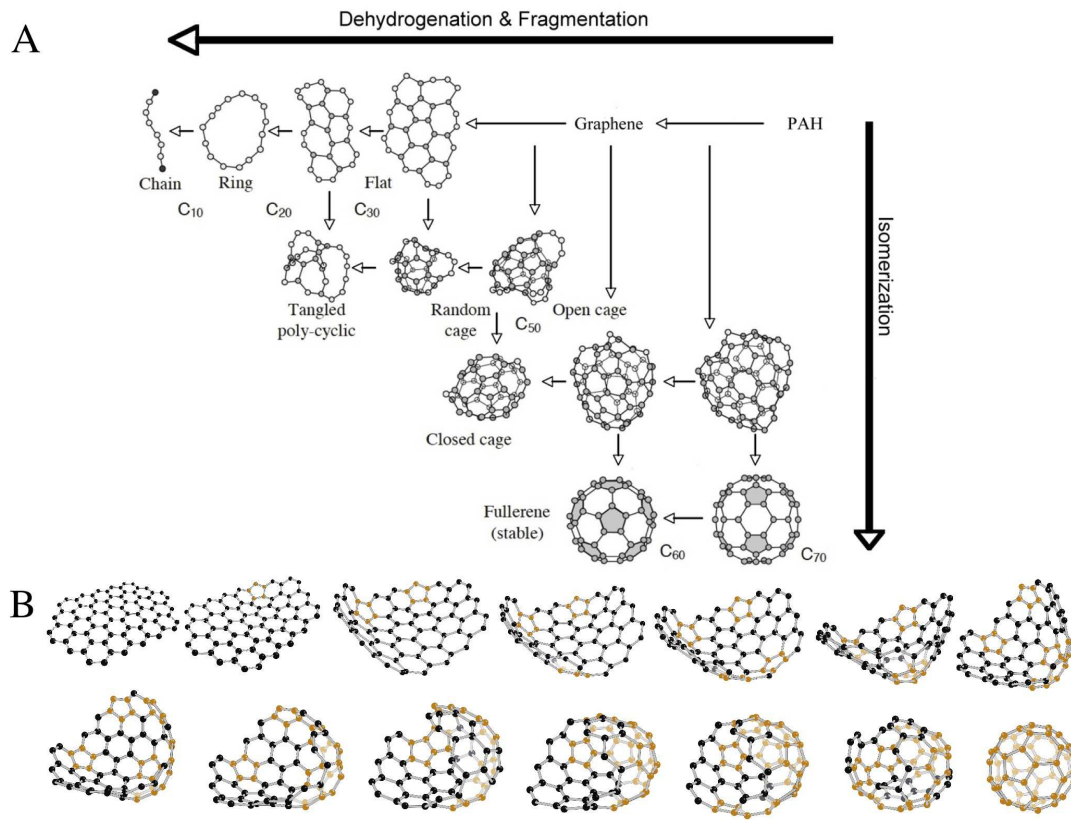


Figure 3.3: Schematic representation of the conversion of PAHs to fullerenes. A: Under strong UV radiation the PAH (top right corner) loses its hydrogen and forms graphene flakes and smaller structures. Carbon loss leads to the formation of pentagons and local curvature. The structures isomerises and arranges into cages. B: An illustration of a possible conversion of a graphene flake to C₆₀. Pentagons are shown in orange. Picture from [2].

3.3 Detection

Detection of the fullerenes is primarily done by analysis of spectra taken with telescopes. An example of such a spectrum obtained from an observation is shown in figure 3.4. The fullerenes are most abundant near a UV source, here the star HD 200775.

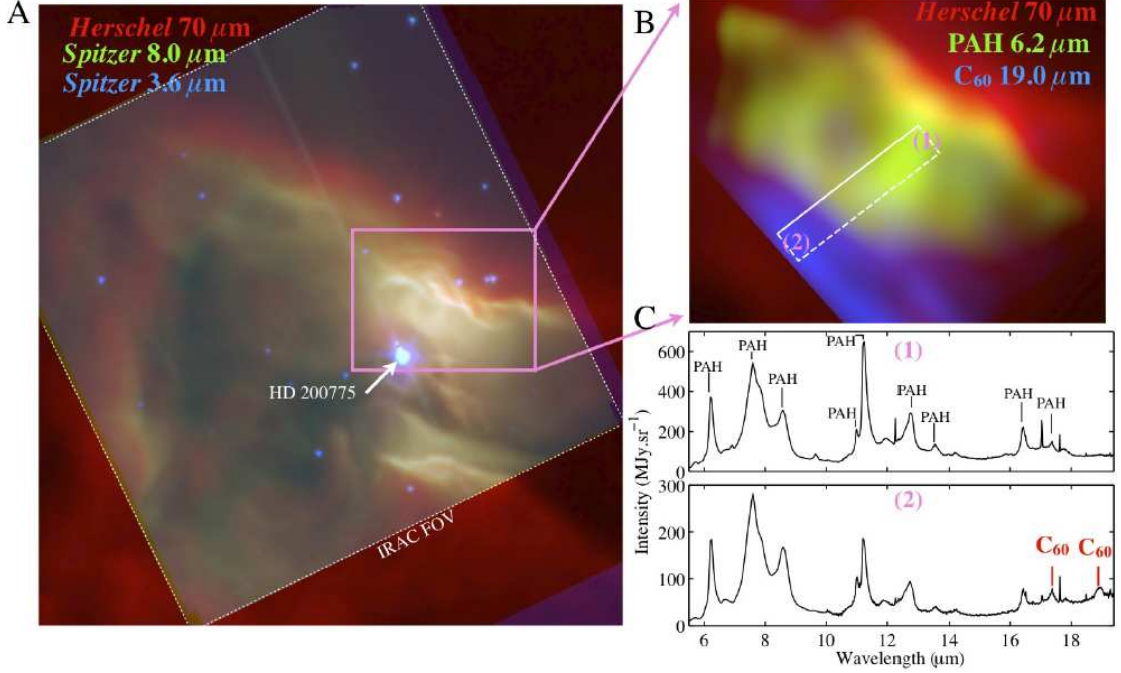


Figure 3.4: Observation of the NGC 7023 nebula in the infrared. A: Colour coded view for three spectroscopes on board of Herschel and Spitzer space telescopes. The young star HD 200775 illuminates the nebula. B: Close up of (A) with blue C₆₀ signature at 19.0 μm or 526 cm^{-1} . The white rectangle shows the region where spectra were obtained. C: Mid-infrared spectra taken at positions (1) and (2) in (B). The PAH peaks and the C₆₀ peaks are indicated. Close to HD 200775 (2) the C₆₀ is more abundant. Picture from [2].

In the infrared band, the modes are associated with typical vibrational excitations. We can distinguish between IR active modes and Raman modes. In the former, a photon is absorbed by the lattice creating a phonon with the same energy. The latter involves a scattering process where the energy of the incoming photon is redistributed in the lattice. By assigning a certain frequency to a vibrational mode one is able to identify the source of the light. For example, the C–C bond is associated with a 1600 cm^{-1} vibrational mode and the C–H stretching can be found at 3100 cm^{-1} . By combining the different peaks of the spectrum one is able to deduce the observed structure. In figure 3.5 we see the Spitzer spectrum of Tc1, a young planetary nebula enshrouding a white dwarf. The active infrared emissions of C₆₀ and C₇₀ are identified. The strongest IR peaks of C₆₀ are at 529, 575, 1176 and 1423 cm^{-1} . We will see these frequencies again when we study the Vibrational Density of States of carbon systems.

Since the two proposed pathways to fullerenes follow different intermediate stages, it would be desirable to determine the production process by following the evolution of the spectrum. In the top-down process, pentagons are formed by carbon loss under UV radiation. Is it possible

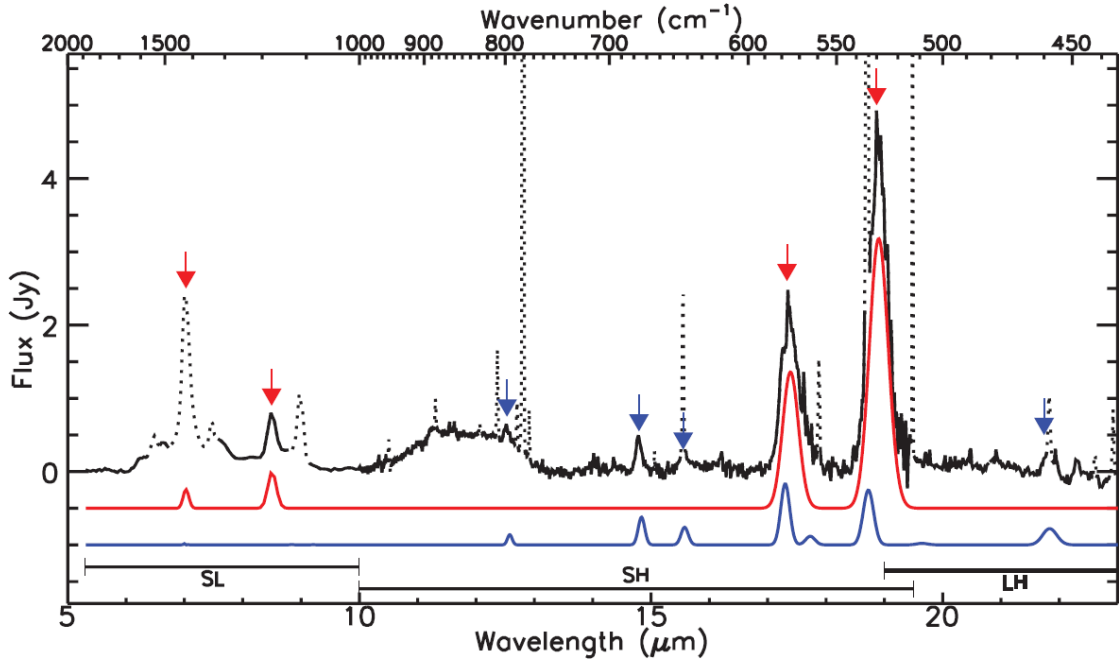


Figure 3.5: The Spitzer Infrared Spectrograph (IRS) spectrum Tc1. The IR peaks of C₆₀ are marked by red arrows, the four strongest IR peaks of C₇₀ by blue arrows. From the linewidth of the peaks the temperature can be fitted. This gives temperatures of 330 K and 180 K for the C₆₀ and C₇₀ respectively. Other features that can be identified are a plateau of SiC at 769 to 909 cm⁻¹ and a 435 cm⁻¹ peak of MgS. Picture from Cami et al. [4].

to see the creation of the pentagons in the spectrum? And does the induced curvature have an effect on the relative position and intensity of the modes? To answer these questions we must be able to quantify the curvature and calculate the spectra. This is done in the two following chapters.

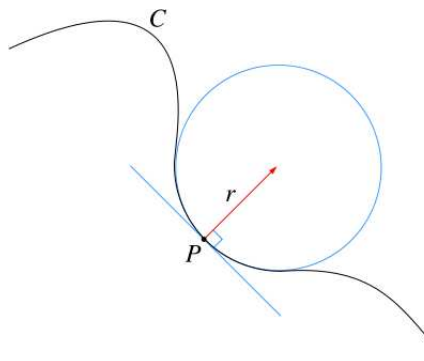
Chapter 4

Curvature

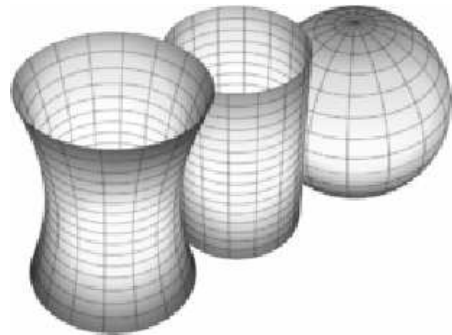
4.1 Continuous curvature

4.1.1 An intuitive approach

We all have an intuitive feeling of what we mean with the word “curvature”. It has to do with the way a surface bends at a certain point. A way of defining a curvature that lies close to these thoughts is presented here. Consider a point P on a surface C . We will try to draw a tangent circle that locally follows the surface at P with highest precision. This circle, named the osculating circle from the Latin *osculari*, to kiss, has its centre on the normal at P and has radius r . The curvature κ is then defined as the reciprocal of r . This procedure is shown in figure 4.1a. This definition naturally gives us zero for the curvature of a flat surface and it scales with the radius for a circle. If the normal to the surface is on the same “side” as the osculating circle we speak of a positive curvature, else we call it negative.



(a) Construction of the osculating circle to a surface C at point P . The centre of the circle lies on the normal at P . The curvature is given by $\kappa = 1/r$.



(b) Three curved surfaces. From left to right: Hyperboloid with $K < 0$; Cylinder with $H = 1/(2r)$ and $K = 0$; Sphere with $H = 1/r$ and $K = 1/r^2$.

Figure 4.1: Defining curvature. **a:** the construction of the osculating circle, **b:** examples of curvature.

For a two dimensional surface we can repeat this procedure. The minimal and maximal curvatures are named the principal curvature and are combined to produce a general curvature at a point: the Mean curvature H and the Gaussian curvature K :

$$H = \frac{\kappa_{min} + \kappa_{max}}{2} \quad , \quad K = \kappa_{min} \cdot \kappa_{max} . \quad (4.1)$$

These measures for curvature are used to classify curvature in surfaces. A few examples of curved surfaces are show in figure 4.1b and figure 4.3.

4.1.2 Mathematical refinements

The notion of curvature given in 4.1.1 is very intuitive but there is a more rigorous way of deriving it. Consider a smooth¹ surface S embedded in a three dimensional space. Every point p (with associated vector \mathbf{p}) on S has a parametrisation from the open set $V \subset \mathbb{R}^2$ given by

$$\mathbf{p}(u, v) = (x(u, v), y(u, v), z(u, v)) \quad (4.2)$$

where u and v are the coordinates within V . If V is smooth we can use the spatial derivatives to calculate the tangent vectors of p in S :

$$\mathbf{p}_u = \left(\frac{\partial x}{\partial u}, \frac{\partial y}{\partial u}, \frac{\partial z}{\partial u} \right) \quad , \quad \mathbf{p}_v = \left(\frac{\partial x}{\partial v}, \frac{\partial y}{\partial v}, \frac{\partial z}{\partial v} \right) .$$

For regular surfaces, the cross product $\mathbf{p}_u \times \mathbf{p}_v$ is never zero and we can define the normal to the surface at point p as

$$\mathbf{n}(p) = \frac{\mathbf{p}_u \times \mathbf{p}_v}{|\mathbf{p}_u \times \mathbf{p}_v|}(p) .$$

Now consider a vector \mathbf{w} in the tangent plane of S in the point p : $\mathbf{w} \in T_S(p)$. If we look at the dot product of \mathbf{w} with \mathbf{n} , it would be zero by construction i.e. $\mathbf{w} \cdot \mathbf{n} = 0$. However, if the surface S has curvature at p , then for small deviations in S from point p the normal will change its relative angle with \mathbf{w} . Thus, the (normal) curvature is defined as the result of this changing dot product:

$$\kappa_n = -d\mathbf{n}(\mathbf{w}) \cdot \mathbf{w} = \kappa \cos(\theta) . \quad (4.3)$$

This construction scheme is depicted in figure 4.2. It gives us the principal curvatures that can be used in equation 4.1. The definitions of the Mean and Gaussian curvature are completely analogous.

¹We could adopt the language of differential geometry and speak of a *manifold* but for our cause more “simplicistic” terms are sufficient.

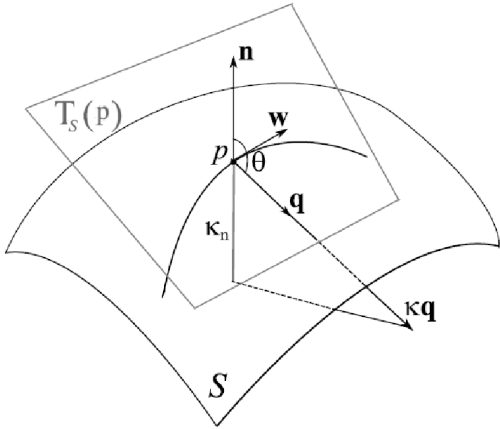


Figure 4.2: Geometrical construction of the curvature vector \mathbf{q} . Plane T is tangent to the surface S at the point p and contains the vector \mathbf{w} . The angle θ between the direction of change of the normal vector \mathbf{n} and \mathbf{w} is the curvature vector $\kappa\mathbf{q}$ where \mathbf{q} is a unit vector in the direction of the curvature. Picture based on figure 2.5 from [24].

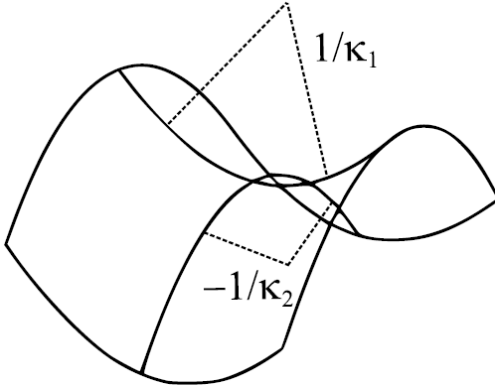


Figure 4.3: Example of a curved space with the two principal curvatures depicted. At this saddle point, one of the curvatures is positive, the other is negative. Hence the Gaussian curvature at this point is negative. If $\kappa_1 = \kappa_2$ the mean curvature is zero. Picture from [24].

4.2 Curvature on a lattice

In the previous section the notion of curvature on a continuous surface was explored. We want to expand the concept in a non-continuous environment. The neat mathematical format of equation 4.3 breaks down since it is impossible to define a derivative on a lattice. We must therefore expand our views on curvature.

The first system that we discuss is the C₆₀ molecule. The atoms form 20 hexagons and 12 pentagons and close in a spherical distribution around the centre of mass (CM). If we model the system by a perfect sphere and find the radius, we can use the idea of the osculating circle to calculate the curvature. For a closed system with N particles we define the radius R as the average distance of the atoms to the centre of mass:

$$R \equiv \frac{1}{N} \sum_i^N \sqrt{(x_i - x_{\text{cm}})^2 + (y_i - y_{\text{cm}})^2 + (z_i - z_{\text{cm}})^2}. \quad (4.4)$$

Calculating the radius of an equilibrated C₆₀ molecule at 0.01 Kelvin gives $R = 3.565 \pm 9.7 \cdot 10^{-4} \text{\AA}$. This results in Mean and Gaussian curvature of $H = 0.2805 \text{\AA}^{-1}$ and $K = 0.0786 \text{\AA}^{-2}$ respectively.

This simple curvature calculation works for closed and compact systems but makes no sense for flat samples. In the following part of this chapter we will present two methods for calculating curvature on a lattice for such systems.

4.2.1 Angle deficit as a measure of curvature

Consider a perfectly flat piece of hexagonal graphene lattice as defined in section 1.2. All angles between an atom and its nearest neighbours are exactly 120° . Any induced curvature will change the angles between the atoms, as shown in figure 4.4. To relate this change in angle to the local curvature, we define the *vertex angle deficit* ϑ_v on an atom site as the difference of the sum of the nearest neighbours angles of the curved configuration compared to this sum in the flat configuration.

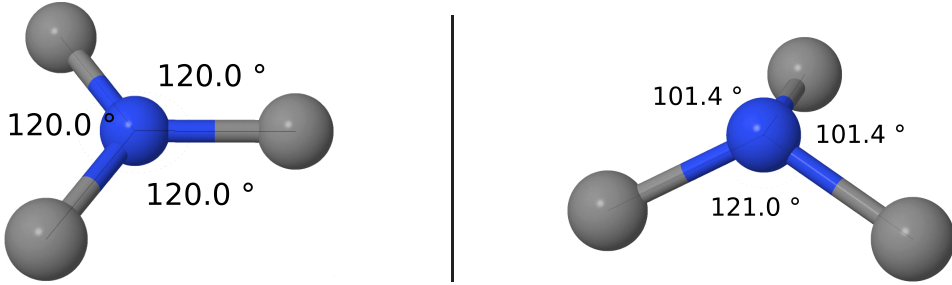


Figure 4.4: Example of how the vertex angle deficit ϑ_v is calculated. Suppose the four depicted atoms normally lie in a plane where the grey particles are at 120° angle with the central blue particle as shown in the left picture. Induced curvature results in the picture on the right where the central atom has been lifted above the plane formed by the other three atoms. The sum of the angles is now $121.0^\circ + 101.4^\circ + 101.4^\circ = 323.8^\circ$. To calculate ϑ_v we have to subtract the sum of the angles in the flat configuration (3 times 120°), so for the blue particle we find $\vartheta_v = 323.8 - 360.0 = -36.2^\circ$.

To illustrate the angle deficits we briefly look back at the C₆₀ molecule. The angles in the hexagons are 120° and those in the pentagons 108° . Since every atom is part of a pentagon and part of two hexagons the angle deficit of the atoms would be $\vartheta_v = -12^\circ$. For a C₆₀ molecule that was thermally equilibrated at 0.01 K we find $\vartheta_v = -12.0 \pm 0.052477$. Since we know the Gaussian curvature of the C₆₀ fullerene from section 4.1.1, ($K = 0.0786 \text{ \AA}^{-2}$) we can use this result as a benchmark when interpreting the vertex angle deficit.

A good model system to study the vertex angle deficit is a ribbon of graphene as shown in figure 4.5. It consists of 80 carbon atoms in a strip like configuration. The long edges have AC configuration, short edges ZZ. The ribbon was brought to thermal equilibrium with a heat bath at 100 Kelvin. This results in a deformed structure with spontaneous curvature.

The C₈₀ AC flake becomes locally curved as a result of thermal fluctuations. The angles between the atoms change and we can see this effect by looking at the vertex angle deficit. As shown in figure 4.6, we see that the deficit is largest at the edge of the sample. Here the interatomic distance that minimises the energy is different from bulk (as explained in section 2.1.1), therefore the edge atoms rearrange, changing their relative angles. The angle deficit here is $\approx +4.36^\circ$. In the bulk of the flake, ϑ_v becomes negative and is, on average, about -0.14° .

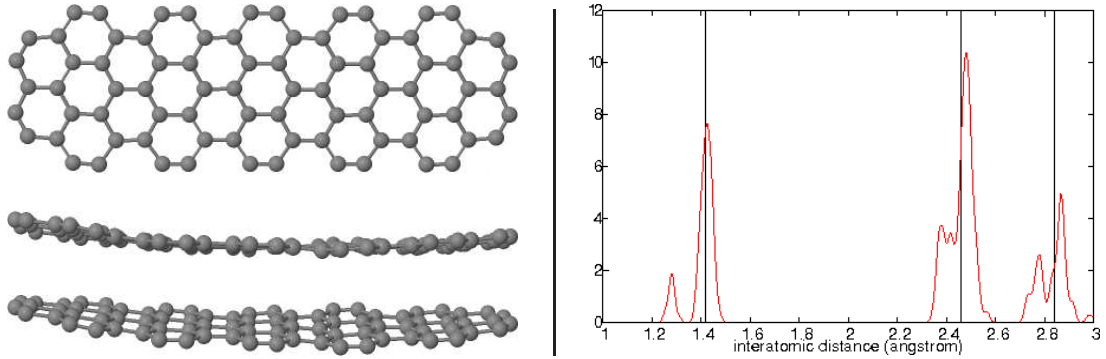


Figure 4.5: The c80 AC flake when it is brought in thermal equilibrium with a heat bath at 100 Kelvin and the edge algorithm active. Left: top, side and slanted view of the flake. Right: Radial distribution function. The vertical lines indicate the interatomic distances in a perfect flat graphene flake.

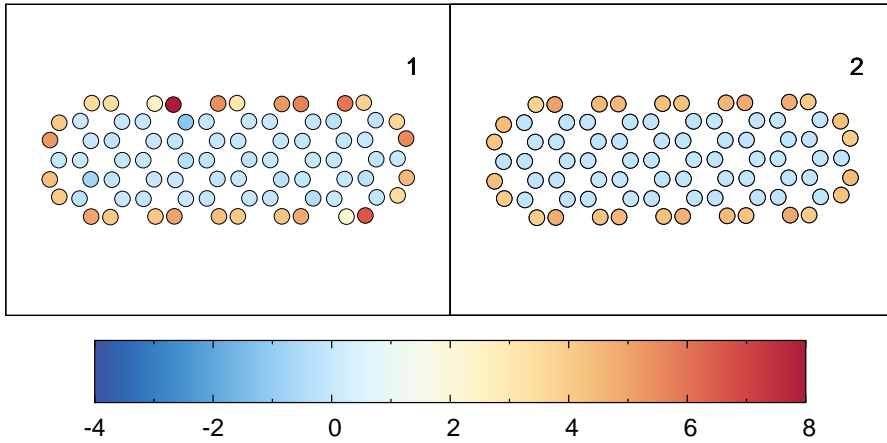


Figure 4.6: Vertex angle deficits for the c80 AC ribbon at 100 Kelvin. 1) deficits for a single configuration. 2) averaged deficit over 100 configurations. The edge and bulk have a well defined mean deficit.

It is clear from the above example that the vertex angle deficit has some success in quantifying curvature on a lattice. It is sensitive to small deformations of the lattice and averages over multiple configurations give precise results. However, we can also identify a few problems. The first problem is the big response of ϑ_v on the local environment of an atom. Because the deficit calculation assumes all angles to be 120° , for an atom at the edge of a flake it naturally gives a nonzero contribution due to the fact that the equilibrium distances differ at the edge from those in the bulk.

Another problem with the vertex angle deficit is the fact that it can have either sign so you have to be careful when taking averages. We illustrate this point in figure 4.7. The vertex angle deficit fluctuates per shown configuration (window 2 to 6) but when we average ϑ_v per site the deficit is well defined (shown in window 7). However, an average over the whole sample would give a value close to zero since the positive contributions compensate the negative. When we use the absolute value to set the sign of the deficit we can see that the deficit increases with temperature, as seen in figure 4.8.

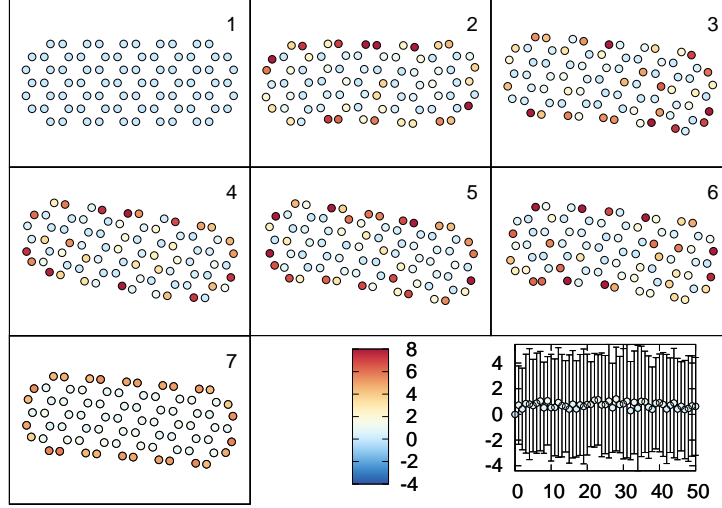


Figure 4.7: The vertex angle deficits θ_v of the c80 AC structure for various configurations from a simulation at 800 Kelvin. 1): initial configuration (flat sample). 2) ... 6) randomly chosen configurations in the simulation. 7) average angle deficit per site. The bottom right corner shows θ_v averaged over all sites in a configuration. We see that while the edge has a distinct nonzero contribution this is counterbalanced by many bulk atoms with a small negative deficit and the average vanishes. The obtained average is thus not only dependent on temperature but also on the ratio of bulk and edge atoms.

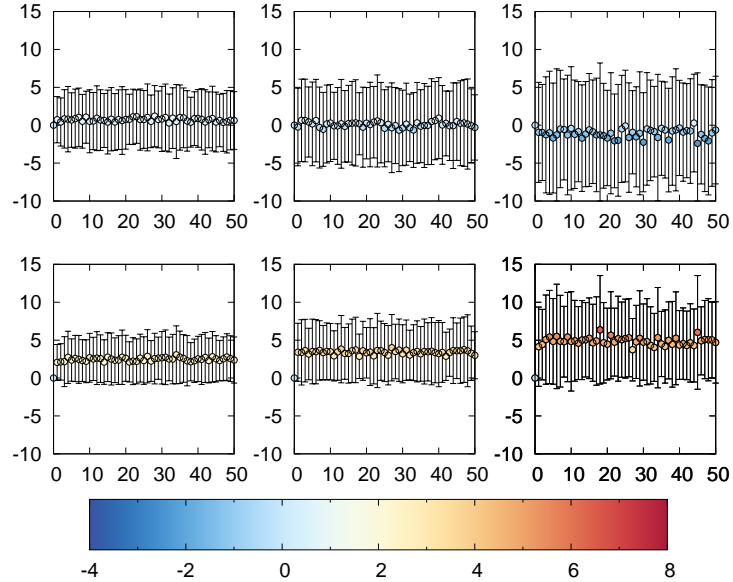


Figure 4.8: Average vertex angle deficits in c80 AC when using deficits of both sign (top row) or only positive (bottom row). Left column: 800K simulation; middle column: 1500K simulation; right column: 2500K simulation. When the deficit is taken with its sign the averaged deficit vanishes whereas if the absolute value of the deficit is used the averaged deficit increases with temperature. The top left graph shows the same data as the bottom right of figure 4.7.

4.2.2 Ring Angle Deficit

Since we consider the carbon atoms on a lattice forming closed rings we can introduce a second kind of angle deficit. For a regular flat polygon of n vertices, the sum of the internal angles α is given by

$$\sum_{i=1}^n \alpha_i = (n - 2) \cdot 180^\circ. \quad (4.5)$$

The angles in the hexagons in graphene thus sum up to 720° and the angles themselves are all 120° . If the rings change their number of vertices (for instance in an edge reconstruction event), the resulting internal angles change accordingly and can be calculated by equation 4.5. Now consider induced curvature. Again, the angles between atoms change and thus the sum of angles in a ring will be different from the flat configuration. We call this difference the *ring angle deficit* ϑ_r . The sign of this angle deficit is always negative. This has to do with the fact that if the angles would add up to a number bigger than $(n - 2) \cdot 180^\circ$, the polygon would not close. Thus, any ring will respond to curvature with a negative angle deficit. The second advantage of the ring angle deficit is the fact that it naturally deals with the changing angles of edge atoms. The vertex angle deficit of the outmost atoms is compensated by other atoms in the ring. Hence, contrary to the vertex deficit, the ring deficit will therefore not respond to the rearrangement of atoms in a plane. We calculated the ring angle deficit for the same 800 Kelvin simulation of C80 AC as in the previous section. The results are shown in figure 4.9. To help comparison we will from now on flip the sign of ϑ_r so it will always be positive.

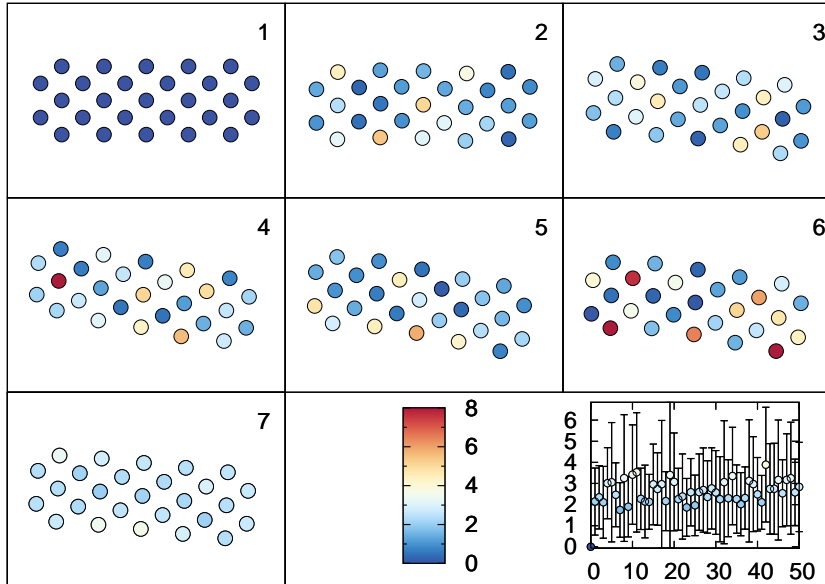


Figure 4.9: The ring angle deficits ϑ_r , taken with a minus sign, of the C80 AC structure for various configurations from a simulation at 800 Kelvin, where every dot represents a ring. 1): initial configuration (flat sample). 2) ... 6) randomly chosen configurations in the simulation. 7) average ring deficit per ring. The bottom right corner shows ϑ_r averaged over all rings in a configuration. The average deficit per ring does not vary much over the whole sample.

The ring angle deficit is not completely without problems. It works very well for flat samples that have some curvature but it cannot handle closed systems like fullerenes. For instance, the hexagons and pentagons of the C₆₀ molecule are all “perfect” i.e. have no deficits so calculating ϑ_r would give zero for the curvature (although $|\vartheta_v| = 12^\circ$).

4.3 Numerical evaluation of curvature

To enable us to classify the curvature of many different systems we have implemented both calculations of curvature on lattice defined in section 4.2.1 and 4.2.2 in a C++ computer code. The program takes a set of configurations as input and calculates the vertex and ring angle deficits for all atoms and rings in all configurations. It gives averages per site/ring over the whole sequence of configurations and gives a global average per configuration. This makes the code ideal to study simulations that include processes that induce curvature like pentagon formation and temperature effects.

In the calculation of the ring angle deficit we first had to identify the ring structures in a configuration. This is not a trivial task since you are only provided with the position of the atoms. We have implemented a ring finding algorithm based on the python program POLYPY written by Jaap Kroes [19] in our code. This uses a recursive function to find all rings in a configuration. The object oriented nature of C++ enables us to follow a ring during the simulation and keep track of its deficit.

To aid projection of a configuration on the 2D plane we have added an algorithm that computes the principal moments of inertia by a calculation of the inertia tensor. We can then rigidly rotate the sample over any desired angle and restore the original orientation of a flake after it experienced a free rotation during a simulation.

4.4 Temperature and curvature

Now that we have a number of tools to evaluate curvature on a discrete lattice we want to use them to describe the effects of temperature on a sample. Since a higher temperature is associated with more local curvature we can see if our definitions follow this intuitive notion. The C₈₀ AC sample was equilibrated at various temperatures and vertex and ring angle deficits were computed. Results were averaged over all atoms/rings and all configurations. Figure 4.10 shows the dependence of the angle deficits on temperature. For ϑ_v the deficits were all taken positive.

We see that the angle deficit grows linearly with temperature. Although the spread grows with temperature the fit stays close to the averaged value. The vertex angle deficit ϑ_v intersects the vertical axis since the edge atoms rearrange themselves even in a perfectly flat sample. The value of ϑ_v at zero temperature is determined by the edges in the $T = 0$ flat configuration.

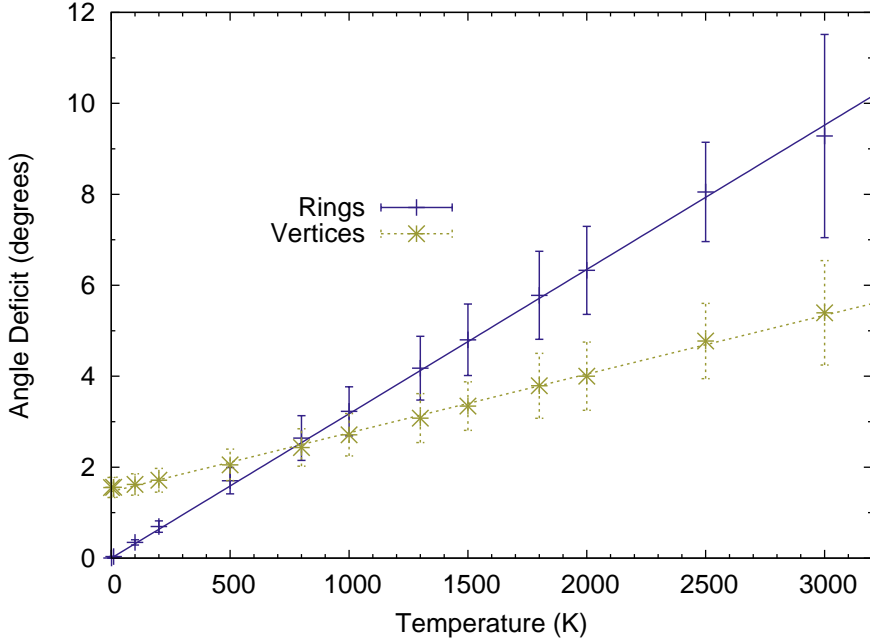


Figure 4.10: Angle deficits per atom to temperature for the C80 AC structure. In blue the ring deficit ϑ_r , in green the vertex deficit ϑ_v . Linear fits are shown (see table 4.1 for the values). Each point is a result of an average over fifty configurations. The vertex deficit does not hit zero at low temperature due to sensitivity to edge modifications.

To test the supposed linear dependence of the deficits we look at a few other systems. Three zigzag terminated graphene flakes with constant width were studied: c80 zz, c104 zz and c120 zz. We also looked at two bigger armchair terminated samples (c158 AC & c172 AC) and a more “circular” flake of 96 atoms: c96 c. The studied structures are shown in figure 4.11.

For all of the mentioned structures we performed MC simulations in the canonical ensemble for fifteen different temperatures. In each simulation a perfect flat flake was brought to the desired temperature. From the configurations generated by the simulation we calculated the average vertex and ring deficits per configuration. These were subsequently averaged over all configurations. The results are shown in figure 4.12 and 4.13.

We see that the ring angle deficit has a linear dependence on temperature for all structures. We have fitted the ring deficit data with a linear function. For clarity we do not plot the fits themselves. Fitting parameters are presented in table 4.1. Up to high temperatures the fits remain close to the data. The three zigzag terminated structures give the same slope of $3.64 \cdot 10^{-3} {}^\circ/\text{K}$. The slope fitted for the armchair flakes varies within 3% of their mean.

For the vertex deficit (Fig. 4.12) a linear fit has less clear results. Whereas the armchair terminated structures seem to behave regularly, the zigzag terminated flakes give erratic data. This becomes more apparent with increasing temperature. This is mainly because the edge atoms start to rearrange, breaking bonds and thus the angles become very irregular. The ring deficit (Fig. 4.13) does not have this problem since a ring disappears when a bond that constitutes the ring is broken.

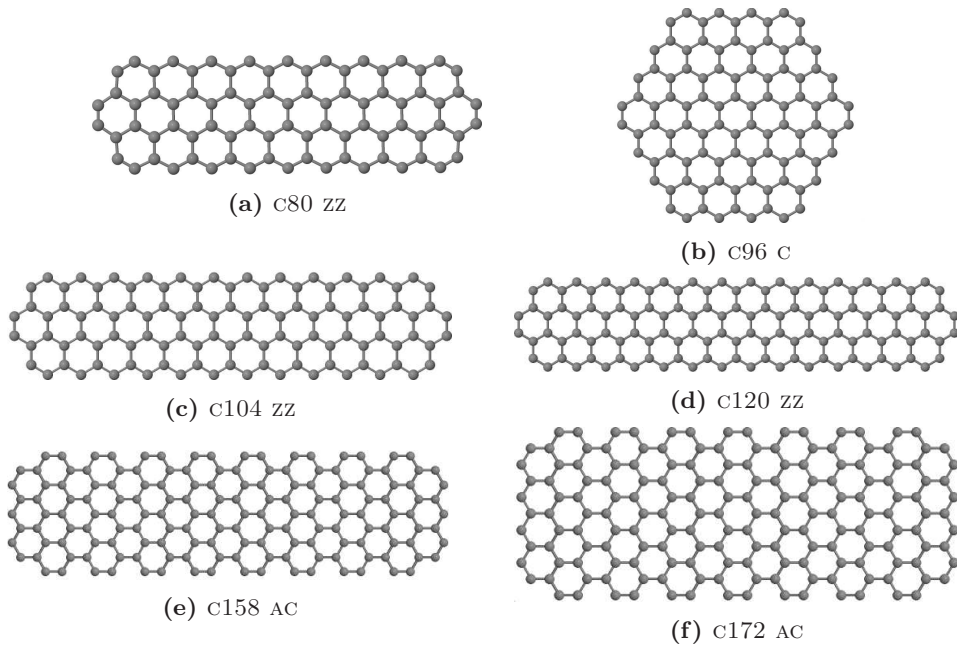


Figure 4.11: The other carbon systems that were studied.

The value of the vertex deficit for all samples at $T=0$ was calculated by a linear fit over the data at temperatures $\leq 100\text{K}$. The specific value is given by the termination of the flake in relation to its size.

Since the ring deficit has the same behaviour at $T=0\text{ K}$ for all structures and it gives good results at high temperatures we will use this notion of curvature for the rest of our analyses of curvature.

Structure	Ring angle deficit slope ($^{\circ}/\text{K}$)	Vertex angle deficit y-intercept ($^{\circ}$)
c96 C	$3.11 \cdot 10^{-3} \pm 2.48 \cdot 10^{-5}$	1.14 ± 10^{-3}
c80 zz	$3.64 \cdot 10^{-3} \pm 2.17 \cdot 10^{-5}$	1.70 ± 10^{-3}
c104 zz	$3.64 \cdot 10^{-3} \pm 5.82 \cdot 10^{-5}$	1.67 ± 10^{-3}
c120 zz	$3.64 \cdot 10^{-3} \pm 3.83 \cdot 10^{-5}$	1.63 ± 10^{-3}
c80 AC	$3.10 \cdot 10^{-3} \pm 2.19 \cdot 10^{-5}$	1.54 ± 10^{-3}
c158 AC	$2.98 \cdot 10^{-3} \pm 9.93 \cdot 10^{-6}$	1.18 ± 10^{-3}
c172 AC	$2.95 \cdot 10^{-3} \pm 1.24 \cdot 10^{-5}$	1.04 ± 10^{-3}

Table 4.1: Values for fitted line for the deficits of the five structures. The ring deficit data was fitted with a linear function through the origin because of the definition: at zero temperature there is no ring deficit. The y-intercept for the vertex angle deficit was obtained by fitting the data up to 100K.

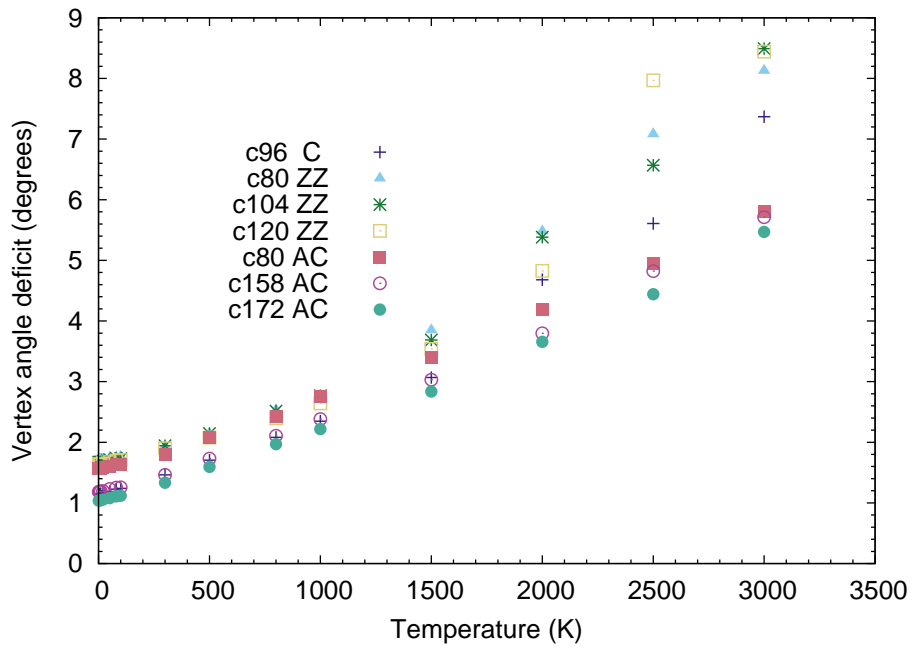


Figure 4.12: Vertex angle deficit as a function of temperature for the seven indicated carbon structures.

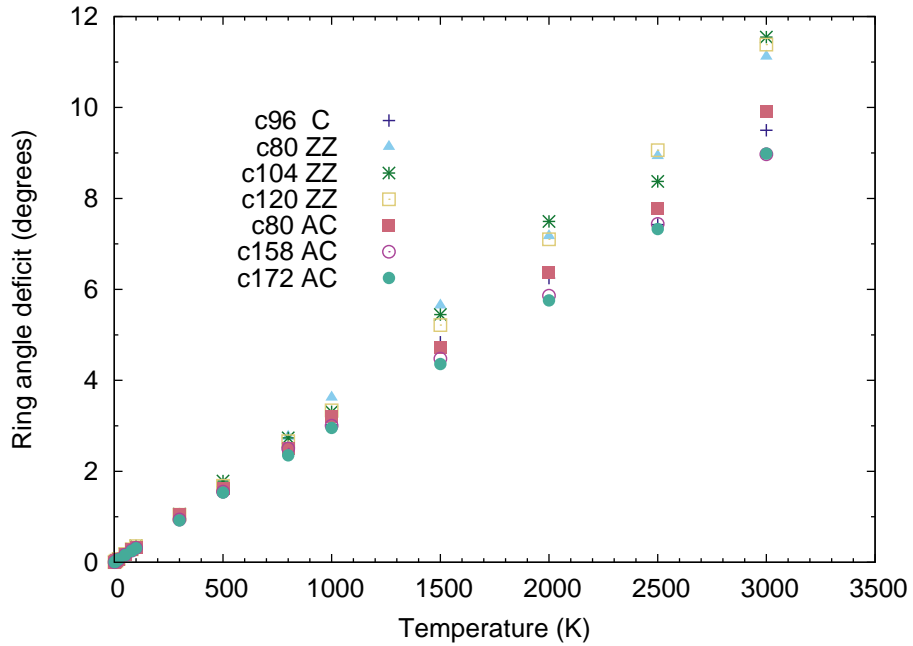


Figure 4.13: Ring angle deficit as a function of temperature for the seven indicated carbon structures.

4.5 Curvature induced by atom loss

In the top-down pathway in the production of fullerenes described in section 3.2, carbon loss due to radiation plays a big role. Due to pentagon formation when a carbon atom is removed from the sample, the system curves and tends to fold up. Chuvalin et al. [6] showed that this can indeed happen to graphene flakes on a carbon substrate under an 80-keV electron beam. The electrons chip away carbon atoms at the edge and induce local curvature. Figure 4.14 shows a model of a graphene flake changing into a fullerene by electron bombardment. A pristine graphene flake **a** suffers carbon loss and becomes the flat structure **b**. Specific atoms at the “armpit” corner get expelled and two pentagons are formed, inducing curvature as seen in **c** & **d**. When the edge zips up we end up with the bowl shaped structure **e**. The remaining open edge is viable to further carbon loss and thus the process continues. When the system has formed a fully closed cage, further etching is suppressed since we have no open edges anymore. Since a random cage is thermodynamically less favourable, isomerisation by a series of Stone-Wales rearrangements [33] leads to perfect fullerenes **f**. Energies associated with this process were calculated with the DFT quantum chemistry package Q-CHEM [6].

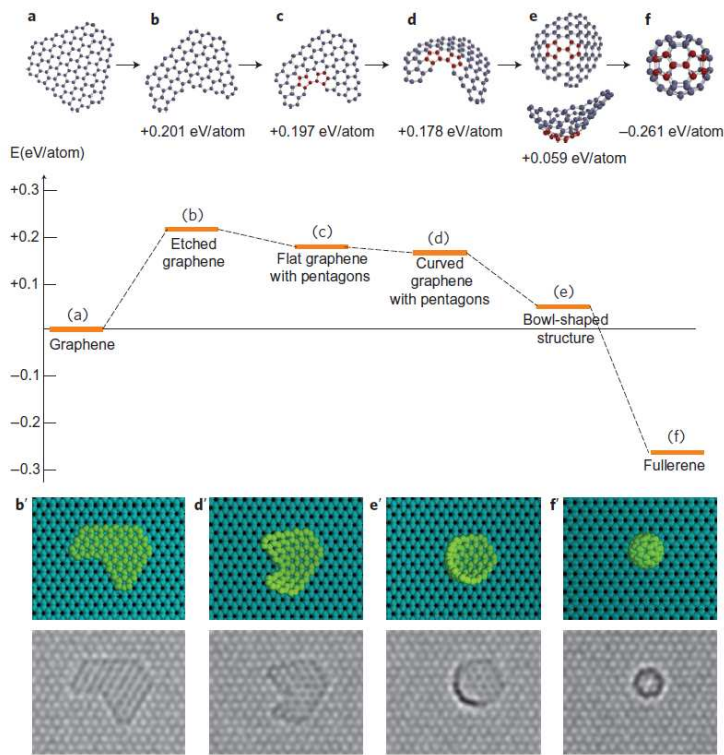


Figure 4.14: A example of a top-down transition from a flat flake to a fullerene. Top row: schematic overview of the process; the intermediate steps are labelled alphabetically. Induced carbon loss at the edge creates curvature; eventually leading to a bowl shaped structure. The bowl edges zip up to form a fullerene. Middle row: Graph of the energy of subsequent structures. Bottom row: simulated Transmission Electron Microscopy (TEM) images corresponding to the shown structures. Picture from [6]

We have tried to simulate the process of figure 4.14 by starting with flake **b**. We brought the flake to thermal equilibration at 300 Kelvin by a MC simulation. Then we removed one atom in the flake located at the armpit bend in the edge of the flake. Subsequent equilibration resulted in a single pentagon (we will refer to the resulting structure as **b'**, since it is an intermediate step between **b** and **c**). This process was repeated to create **c** with two pentagons, seen in red in figure 4.14. It must be noted however that **c** was not at all flat since there is some induced curvature due to the first pentagon. This makes the transition between **c** and **d** not well defined. This flake eventually curves into structure **d**. However, the edges of the flake are not adjacent enough to zip-up. To achieve this we had to manually displace many atoms to be more close together. The zipped up system **e** was bowl shaped with two pentagons providing the curvature.

Figure 4.15 shows the energy of the flake during this simulation. The energies of all curved stages is higher than the energy of the flat flake **a** in accordance with Chuvalin et al. [6]. However, the energies of the stages **c** and **d** are not significantly lower than the energy of **b**, contrasting their results. Furthermore, the energy gain from **d** to **e** is less in our calculations.

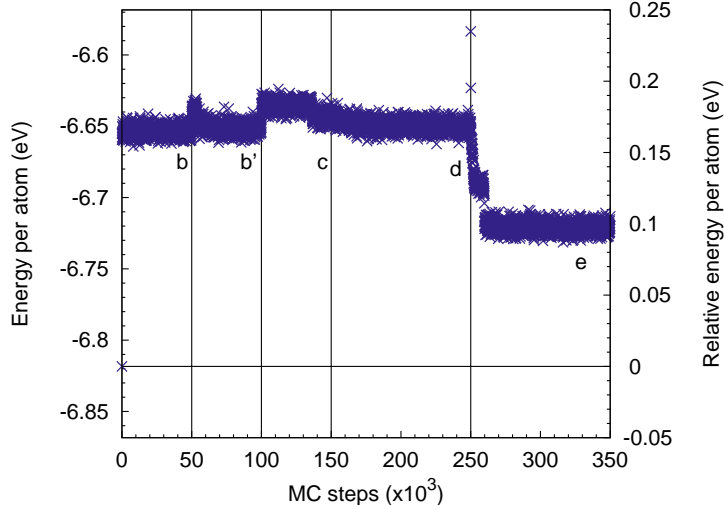


Figure 4.15: Energy per atom of the bowl formation in a 300 Kelvin simulation. Left axis gives the absolute energy, the right axis the energy relative to **a**. The vertical lines indicate the transition from one of the intermediate shapes to another. At the first and second line (**b** → **b'** & **b'** → **c**), an atom was removed, eventually creating a pentagon. At the fourth line (**d** → **e**) the atoms in the sample were *manually* displaced to zip up the edge. Note that the displacements resulted in a configuration with a higher energy (0.5 eV) than the bowl shaped system **d**.

To move the atoms of **d** close enough to get the zipping effect extra bending had to be manually introduced in the sample. This led to very high energy states seen in figure 4.15 because the atoms were displaced from their equilibrium position. Since this is thermodynamically unfavourable the possibility for this to happen by itself gets very small. Under constant radiation it is thus more likely that another carbon atom gets removed before the edges can meet. One must bear in mind that the location of the carbon loss is very important for the formation of a closed system. If the wrong atom is chipped away, curvature in the wrong direction can be induced or the flake loses its graphitic nature. The need for more carbon loss thus limits the yield of closed cages in the top-down production pathway.

4.5.1 Analysis of the curvature

Given the tools in describing curvature presented previously, we can analyse the emergence of curvature in the process described in [6]. In figure 4.16 we have averaged the ring angle deficit ϑ_r per ring over the configurations in the simulation. The jumps in energy in the simulation helped us to isolate the configurations that had a similar structure.

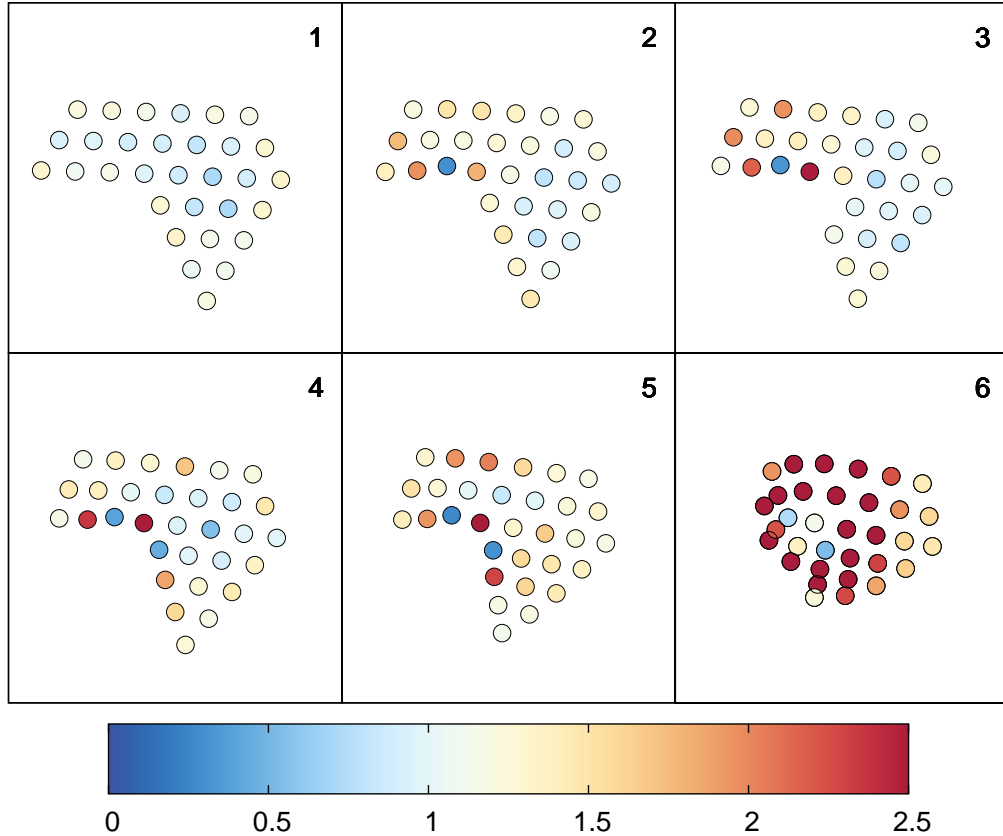


Figure 4.16: Ring angle deficits averages in a 300 Kelvin simulation. Note that the nature of the rings (hexagon or pentagon) cannot be directly seen. 1) flake **b**. 2) flake **b'**, the flake has one pentagon. 3) intermediate state with one pentagon and one “open ring”. 4) flake **c**, two pentagons are present. 5) flake **d**, we have two pentagons and a curved structure. 6) flake **e** after zipping; we see much curvature around the two flat pentagons. The projection of the sample on the xy-plane gets subsequently poorer as the sample folds.

The origin of the curvature in the flake is very clearly visible. When the sample is flat, all rings have a minor nonzero deficit contribution. When we introduce a pentagon by atom loss, this ring remains flat (dark blue dot in window 2 of figure 4.16) but the hexagons around it curve, indicated by the orange colour. Removing one additional atom results in a configuration where the missing carbon atom leaves a rings structure open (missing dot in window 3). The adjacent hexagon reacts with a high curvature (red); it keeps the structure together by bending the top-left part downwards. This extra bending eventually creates the second pentagon. It also remains flat while the hexagons bend further. After the zipping of the flake many hexagons have a large curvature. However, the two pentagons have almost zero deficit.

Pentagons are able to induce local curvature when they are created by carbon loss at the edge of a flake. If multiple of such curvature hot spots are located near each other it can result in a bowl like structure. Such global curvature can bring edges close together and thus initiate zipping; closing a flake to form a cage. The pentagons concerned remain flat whereas the hexagons that are adjacent are responsible for the curvature. The ring angle deficit is a good tool to visualise the transition from a flat to a closed system.

4.6 More pentagon related curvature

In the previous example, the curvature was induced by pentagons in a process where atoms were etched away from the system. There are two other simple ways to create pentagons in a sample. The first one is by an edge reconstruction event at the zigzag edge of a graphene flake. As explained in section 2.1.1, two hexagons rearrange to form a pentagon-heptagon pair. Another possible source of pentagons is the Stone-Wales defect. Two carbon atoms rotate their position by 90° with respect to their initial bond thus creating two pentagons and two heptagons from four hexagons. Figure 4.17 shows two examples of both defects. The configurations were taken from a 0.01 Kelvin simulation.

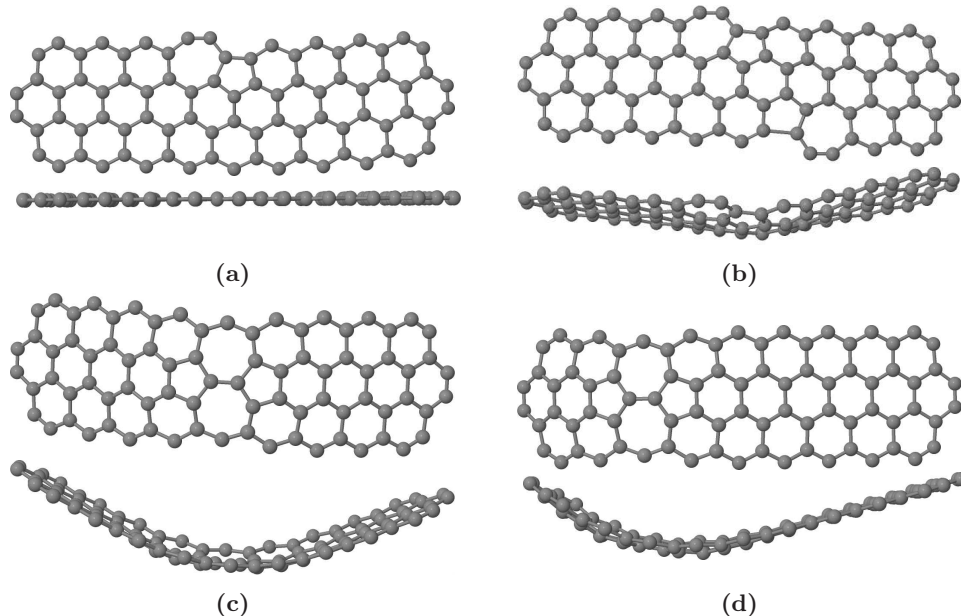


Figure 4.17: Equilibrium configurations at 0.01K for four defected c80 zz structures; top and side view. (a) single edge reconstruction; (b) double edge reconstruction; (c) sw defect in the centre of the flake; (d) sw defect at the side of the flake.

The sample with one edge reconstruction remains flat despite the pentagon. However, when we add another edge reconstruction, the sample begins to buckle and start to form a bowl in between the two defects. A single sw defect has a profound effect on the curvature. In figure 4.18 we show the ring angle deficit for these structures.

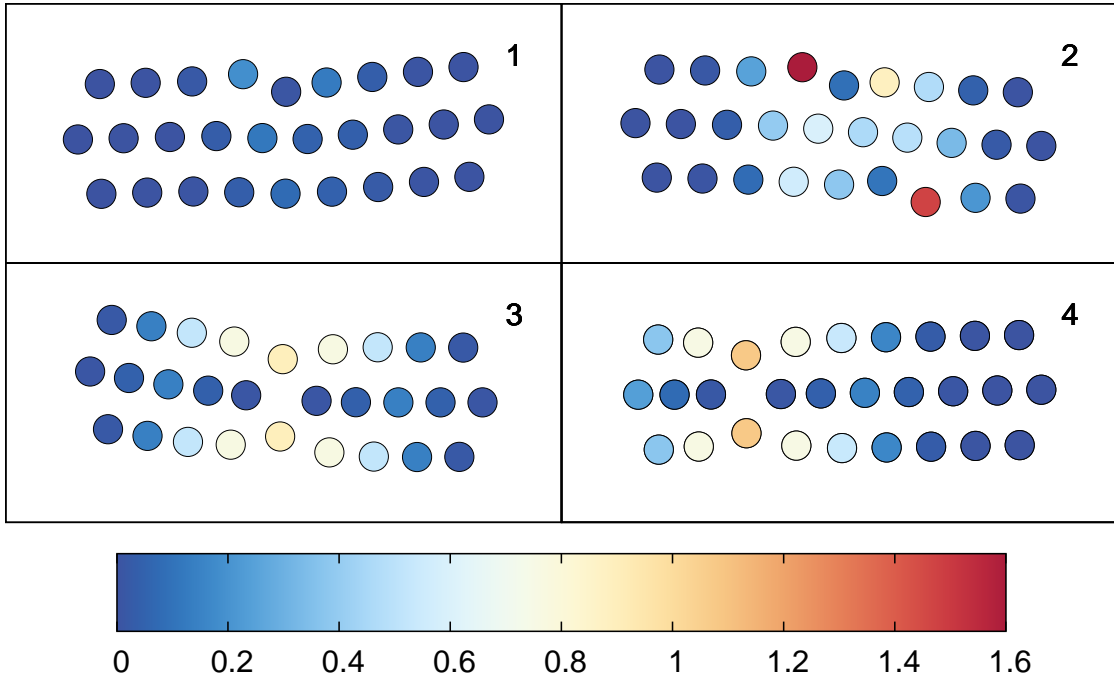


Figure 4.18: Ring angle deficits for the defected flakes shown in figure 4.17. 1) single edge reconstruction. 2) double edge reconstruction. 3) sw defect in the centre of the flake; 4) sw defect at the side of the flake.

As we saw with flake **d**, the pentagons themselves have little angle deficit. The hexagons in their vicinity contribute the most to the curvature. If the induced curvature of a pentagon overlaps with the curvature created by a second pentagon, a global curvature effect becomes visible. Note that while the deficit at the heptagons of the sw defects is quite small ($\approx 1^\circ$), the typical value of ϑ_r for a flat structure at 0.01 K is 10^{-5} degrees so this effect is very strong. We should therefore always be aware at which temperature our sample is equilibrated when we interpret the value of the angle deficit for a given site.

Describing curvature by looking at the angle deficit works well and gives us a grip on the magnitude of curvature of a discrete lattice. The ring angle deficit proves to be more useful when describing low temperature systems since it is less sensitive to edge effects and scales linearly with temperature. With the deficit as tool, we are able to follow the transformation of a flat sample to a curved one and see how local curvature affects the whole sample. The role of pentagons in the formation of curved structures is a delicate one. If the pentagon is not located at the edge of a sample (as with the etched structure **e** or both the C80 ZZ samples with sw defects) high curvature can be expected. When the pentagon is located at the edge, the local environment is important in defining the minimum energy structure.

Chapter 5

Deformations and phonon Density of States

As we have seen in chapter 3, it is possible to identify certain carbon allotropes by their infrared emission lines. The photon energy can be related to phonon excitations of these structures. In this chapter we present results on the phonon spectra of different carbon systems and study the influence of structural deformations such as defects and curvature.

5.1 Theory of lattice dynamics

Consider an infinite layer of graphene. The atoms have a minimum energy position in relation to the other atoms. We allow the atoms to vibrate around these minima. Describing these vibrations results in the quasi-particle description of phonons. Here we present some of the basics of the theory of lattice dynamics and explain how the phonon spectra can be calculated.

In a crystal we can identify a unit cell that is periodically repeated to represent the infinite sample. The basis vectors the the unit cell are \mathbf{a}_1 , \mathbf{a}_2 and \mathbf{a}_3 . All lattice points are located at integer combinations of these vectors. We can therefore introduce the vector $\mathbf{R}_l = l_1\mathbf{a}_1 + l_2\mathbf{a}_2 + l_3\mathbf{a}_3$. Every unit cell contains N atoms labelled by κ , the vector \mathbf{d}_κ gives all atomic positions within the unit cell. An example is given in figure 1.3. If we denote the displacements of the atoms with the vector $\mathbf{u}_{l,\kappa}$ we can write all atom coordinates as $\mathbf{r}_{l,\kappa} = \mathbf{R}_l + \mathbf{d}_\kappa + \mathbf{u}_{l,\kappa}$.

We can expand the potential $V(\mathbf{r}_{l,\kappa})$ around the equilibrium positions

$$V(r_{l,\kappa}^\alpha) = V_0 + \sum_{l,\kappa,\alpha} \left[\frac{\partial V}{\partial u_{l,\kappa}^\alpha} \right]_0 u_{l,\kappa}^\alpha + \frac{1}{2} \sum_{l,\kappa,\alpha} \sum_{l',\kappa',\beta} \left[\frac{\partial^2 V}{\partial u_{l,\kappa}^\alpha \partial u_{l',\kappa'}^\beta} \right]_0 u_{l,\kappa}^\alpha u_{l',\kappa'}^\beta + \mathcal{O}(u^3) \dots \quad (5.1)$$

where the three Cartesian coordinates are indicated by the Greek indices. The leading term at the right-hand side V_0 gives the total potential energy when the atoms are in the equilibrium position and is a constant. Furthermore, since the potential at the equilibrium position is minimal, the second term on the right-hand side vanishes. All the interesting physical phenomena come from the quadratic and higher order terms. Truncating the expansion at the second order results in the *harmonic approximation*. It is a valid assumption when the displacements are small.

The Hamiltonian of the system contains, in the harmonic approximation, a term for the cohesive energy of the equilibrium configuration (the constant V_0), the kinetic energy of the atoms and the quadratic term of equation 5.1. The equation of motion then becomes

$$M_\kappa \ddot{u}_{\mathbf{l},\kappa}^\alpha = - \frac{\partial V}{\partial u_{\mathbf{l},\kappa}^\alpha} = - \sum_{\mathbf{l}',\kappa',\beta} \phi_{\mathbf{l},\kappa;\mathbf{l}',\kappa'}^{\alpha,\beta} u_{\mathbf{l}',\kappa'}^\beta \quad (5.2)$$

where we have introduced the mass M_κ and the force constants ϕ :

$$\phi_{\mathbf{l},\kappa;\mathbf{l}',\kappa'}^{\alpha,\beta} = \left[\frac{\partial^2 V}{\partial u_{\mathbf{l},\kappa}^\alpha \partial u_{\mathbf{l}',\kappa'}^\beta} \right]_0. \quad (5.3)$$

The force constants matrix gives us the force exerted on atom (\mathbf{l}, κ) in the α direction by the atom (\mathbf{l}', κ') when the latter is displaced in the β direction while all other atoms are kept in their equilibrium position [25].

The definition in equation 5.3 satisfies the condition

$$\phi_{\mathbf{l},\kappa;\mathbf{l}',\kappa'}^{\alpha,\beta} = \phi_{\mathbf{l}',\kappa';\mathbf{l},\kappa}^{\beta,\alpha} \quad (5.4)$$

since the order of partial derivatives is arbitrary. Besides this symmetry, the forces must not change when the whole sample is rigidly displaced by any vector \mathbf{v} . This means that when substituting $u_{\mathbf{l}',\kappa'}^\beta$ by $u_{\mathbf{l}',\kappa'}^\beta + v^\beta$, the result must be the same. Using this requirement of translational invariance in equation 5.2 directly implies:

$$\sum_{\mathbf{l}',\kappa'} \phi_{\mathbf{l},\kappa;\mathbf{l}',\kappa'}^{\alpha,\beta} = 0. \quad (5.5)$$

We can also displace the lattice through a lattice translation vector $\mathbf{x}_\mathbf{l}$ i.e. $\mathbf{R}_{\mathbf{l},\kappa} \rightarrow \mathbf{R}_{\mathbf{l},\kappa} + \mathbf{x}_\mathbf{l}$. But since it is a lattice vector we can write:

$$\mathbf{R}_{\mathbf{l},\kappa} + \mathbf{x}_\mathbf{l} = \mathbf{R}_{\mathbf{l}+\mathbf{m},\kappa}. \quad (5.6)$$

Furthermore, the interatomic forces will not change so $\phi_{\mathbf{l}+\mathbf{m},\kappa;\mathbf{l}'+\mathbf{m},\kappa'}^{\alpha,\beta} = \phi_{\mathbf{l},\kappa;\mathbf{l}',\kappa'}^{\alpha,\beta}$. Choosing $\mathbf{m} = -\mathbf{l}$ or $-\mathbf{l}'$ we get

$$\phi_{\mathbf{l},\kappa;\mathbf{l}',\kappa'}^{\alpha,\beta} = \phi_{0,\kappa;\mathbf{l}-\mathbf{l},\kappa'}^{\alpha,\beta} = \phi_{\mathbf{l}-\mathbf{l}',\kappa;0,\kappa'}^{\alpha,\beta} \quad (5.7)$$

and we see that the dependence of the forces on \mathbf{l} and \mathbf{l}' works only via their difference. We will use these symmetry properties of ϕ later on.

Because the lattice is periodic for translations of a lattice vector we expect the solutions to equation 5.2 to share this property. We therefore consider solutions of the form

$$u_{\mathbf{l},\kappa}^\alpha = \frac{u_\kappa^\alpha(\mathbf{q})}{\sqrt{M_\kappa}} e^{i(\mathbf{q} \cdot \mathbf{R}_\mathbf{l} - \omega t)} \quad (5.8)$$

i.e. a plane wave solution with frequency ω , wavevector \mathbf{q} and amplitude $u_\kappa^\alpha(\mathbf{q})$. By substituting equation 5.8 into the equation of motion we end up with

$$\omega^2 u_\kappa^\alpha(\mathbf{q}) = \sum_{\kappa',\beta} D^{\alpha,\beta}(\kappa, \kappa', \mathbf{q}) u_{\kappa'}^\beta(\mathbf{q}) \quad (5.9)$$

where we have defined the *dynamical matrix*:

$$D^{\alpha,\beta}(\kappa, \kappa', \mathbf{q}) = \frac{1}{\sqrt{M_\kappa M'_\kappa}} \sum_{l'} \phi_{l,\kappa;l',\kappa'}^{\alpha,\beta} e^{i\mathbf{q}\cdot(\mathbf{R}_{l'} - \mathbf{R}_l)} . \quad (5.10)$$

It can be easily shown that the dynamical matrix is Hermitian:

$$\begin{aligned} [D^{\alpha,\beta}(\kappa, \kappa', \mathbf{q})]^* &= \frac{1}{\sqrt{M_\kappa M'_\kappa}} \sum_{l'} \phi_{l,\kappa;l',\kappa'}^{\alpha,\beta} e^{-i\mathbf{q}\cdot(\mathbf{R}_{l'} - \mathbf{R}_l)} \\ \stackrel{5.4}{=} &\frac{1}{\sqrt{M_\kappa M'_\kappa}} \sum_{l'} \phi_{l',\kappa';l,\kappa}^{\beta,\alpha} e^{-i\mathbf{q}\cdot(\mathbf{R}_{l'} - \mathbf{R}_l)} \\ \stackrel{l' \rightarrow 2l-l'}{=} &\frac{1}{\sqrt{M_\kappa M'_\kappa}} \sum_{l'} \phi_{l+(1-l'),\kappa';l,\kappa}^{\beta,\alpha} e^{-i\mathbf{q}\cdot(\mathbf{R}_{2l-l'} - \mathbf{R}_l)} \\ \stackrel{5.6 \& 5.7}{=} &\frac{1}{\sqrt{M_\kappa M'_\kappa}} \sum_{l'} \phi_{l,\kappa';l',\kappa}^{\beta,\alpha} e^{-i\mathbf{q}\cdot(\mathbf{R}_l - \mathbf{R}_{l'})} \\ &= D^{\beta,\alpha}(\kappa', \kappa, \mathbf{q}) . \end{aligned} \quad (5.11)$$

Equation 5.9 is a set of $3N$ coupled linear differential equations yielding the amplitudes of the displacements at each frequency. The frequency spectrum is given by the eigenvalue equation

$$|D^{\alpha,\beta}(\kappa, \kappa', \mathbf{q}) - \omega^2(\mathbf{q})\delta_{\alpha,\beta}\delta_{\kappa,\kappa'}| = 0 . \quad (5.12)$$

Since the dynamical matrix is Hermitian, for each value of \mathbf{q} there are $3N$ real solutions for $\omega^2(\mathbf{q})$. This means that $\omega(\mathbf{q})$ is real or purely imaginary. Because the amplitudes of the displacements in equation 5.8 grow exponentially for imaginary frequencies, the lattice is not stable if these solutions occur. This could happen when the studied sample was not in the minimum energy configuration of the potential.

5.2 Phonon calculations with PhononLCBOP

By solving equation 5.12 we can find the phonon frequencies at a certain wavevector. Karssemeijer [14] and Locht [21] wrote an extension to LCBOPII to perform this calculation. This code is a standalone version of LCBOPII and calculates the phonon spectra for a certain configuration of carbon atoms. The force constants are calculated by the finite differences expression of the second derivative equation 5.3. Figure 5.1 shows the dispersion relation $\omega(\mathbf{q})$ for graphene for a high symmetry path in the first Brillouin zone. The different modes are labelled.

From the spectrum we can construct the phonon Density of States ($g(\omega)$ or DOS) by counting the number of modes per frequency interval $\Delta\omega$ for all wavevectors \mathbf{q} . Each contribution was then represented by a normalised Gaussian of width σ around the centre of the interval $\Delta\omega$. Figure 5.2 shows the result for bulk graphene where $\sigma = 10$. We can identify the peaks in the DOS by observing the wavevectors where the dispersion has zero slope.

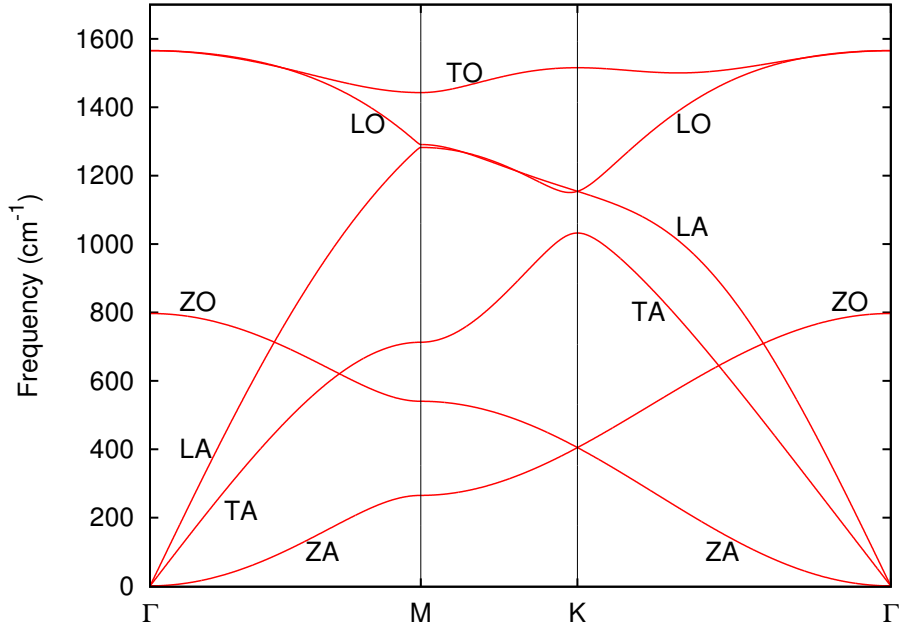


Figure 5.1: The phonon dispersion of graphene as calculated with LCBOPII by Karssemeijer [14]. The horizontal axis constitutes a path through the first Brillouin zone indicated by the letters defined in section 1.2. Acoustic modes (A) and optical modes (o) are identified as well as their direction of displacement (transverse T, longitudinal L or out-of-plane z). Picture courtesy of Karssemeijer [14].

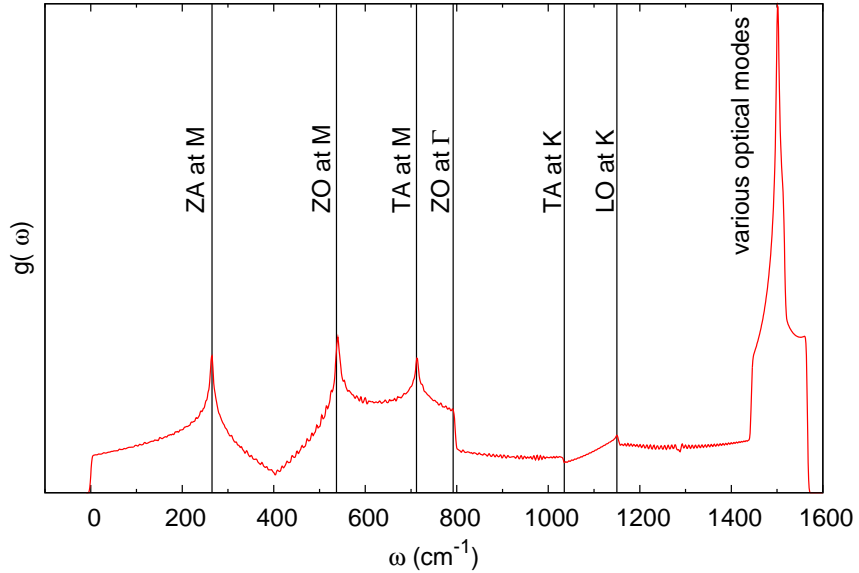
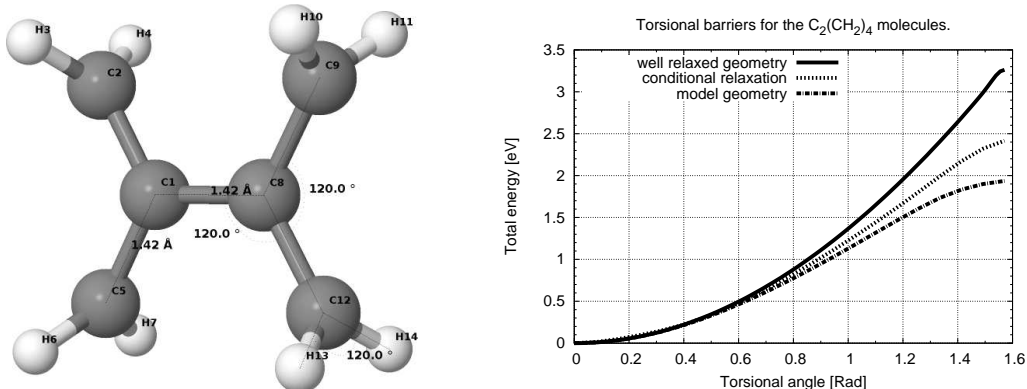


Figure 5.2: Phonon Density of States for graphene. The labels are described in the caption of figure 5.1. The peaks correspond to extrema in the dispersion.

5.2.1 Models of torsion

When a bond in a molecule is twisted the energy increases. This torsional energy penalty typically has a maximum at an angle corresponding to one of the symmetry properties of the molecule. These deformations can result in electronic rearrangements such as changes in hybridisation since they change the local environment of the atoms. These effects therefore affect the bulk behaviour of the system. For instance, it has been shown by Wu et al. [35] that the liquid phase of carbon can only be correctly described when torsion is included. If the torsion is not correctly taken care of, a fictitious liquid-liquid phase transition can be observed.

It can be easily understood that conjugation of electrons in carbon bonds is strongly dependent on the torsion angle. Since LCBOPII assumes a local environment for a certain atom to calculate the bond order and conjugation, the accuracy of the program highly depends on the energy cost to put such a neighbourhood under torsional stress. A good description for the torsional energy barrier is thus important. A study into this energy barrier for three fold coordinated carbon was performed by Akhukov et al. [1]. By rigid rotation of one half of a symmetric molecule they were able to calculate the torsional energy barrier for different geometries. Figure 5.3b shows results for the torsion energy barrier for three different realisations of a $C_2(CH_2)_4$ molecule. The molecule was created in a model graphitic geometry (depicted in figure 5.3a) with a central C – C of 1.42 Å and 120 degrees angles between the atoms. By twisting without changing the internal distances, an energy barrier of 1.92 eV was found. If the sample is relaxed, the energy barrier increases considerably. This higher barrier however is not representative for a graphitic system because the central bond length in the cell decreased to a length typical for a double bond. The torsion energy barrier is very sensitive to the structure of the system.



(a) Model geometry of the $C_2(CH_2)_4$ molecule. The central C – C bond for this geometry is graphitic i.e. has a length of 1.42 Å.

(b) Torsional barrier for rotations around the central bond of the $C_2(CH_2)_4$ molecule. Results for three realisations are depicted. Picture courtesy of Akhukov et al. [1].

Figure 5.3: The structure (a) and torsional barrier (b) of $C_2(CH_2)_4$. The model geometry has a graphitic central bond whereas the relaxed structures have more of a double bond. Because of the symmetry of the structure, the rotation is only required to go from 0 to $\pi/2$.

From this one can see that the problem is complex; further study has led to a new form of torsion in LCBOPII where the energy costs of the torsion is fitted to ab-initio calculations [10].

Effects of new torsion on phonon Density of States

Since the torsion term in LCBOPII changes the energy it can have an effect on the phonon spectra. In figure 5.4 we compare the DOS of bulk graphene with the old and the new torsion.

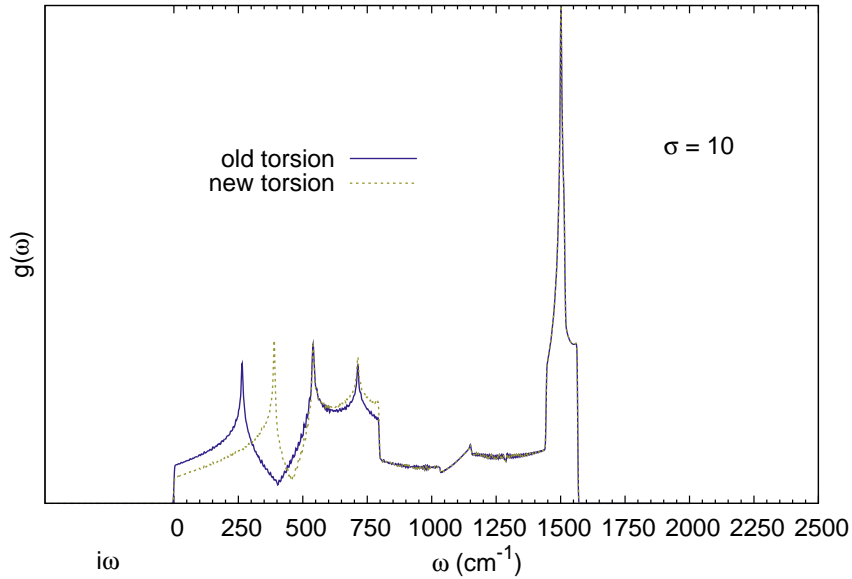


Figure 5.4: Comparison of the phonon DOS ($\sigma = 10$) for bulk graphene with the old (solid blue) and new torsion (dotted green) term in LCBOPII. The low frequency modes (typically out of plane) shift to a higher frequency. The high frequency modes (typically in plane) are not affected.

The new torsion stiffens the modes below $\omega \lesssim 800 \text{ cm}^{-1}$ and leaves higher modes unaffected. This can be understood by an analysis of the displacements for phonon modes with small ω . These modes typically have an out-of-plane component and thus induce a torsional component in the atomic bonds. The modes with $\omega \gtrsim 800 \text{ cm}^{-1}$ are commonly in-plane and therefore do not incur a torsional energy penalty.

The effect of the new torsion on three different systems is shown in figure 5.5. The first is the well known C₆₀ fullerene, the second is the C₈₀ AC structure that was extensively studied in chapter 4 and the third is a circular flake of 54 carbon atoms, a smaller version of the C₉₆ C sample and shown in the appendix A on page 59 called C₅₄ C. The C₈₀ AC and the C₅₄ C structure are flat whereas the C₆₀ molecule forms a closed cage. Both flat systems resemble the situation in bulk graphene: the low frequency modes drift to higher ω but the DOS is the same for $\omega \gtrsim 800 \text{ cm}^{-1}$. The C₆₀ fullerene shows the shift in frequencies for the low ω modes but the DOS at higher frequencies also shows a different spectrum. This is explained by the fact that the torsional part of the energy is nonzero for the equilibrated structure. In a closed cage, the bonds between the atoms are always under some torsional stress.

Later in this report we will discuss the other features that can be seen in these figures, particularly the presence of the imaginary frequencies.

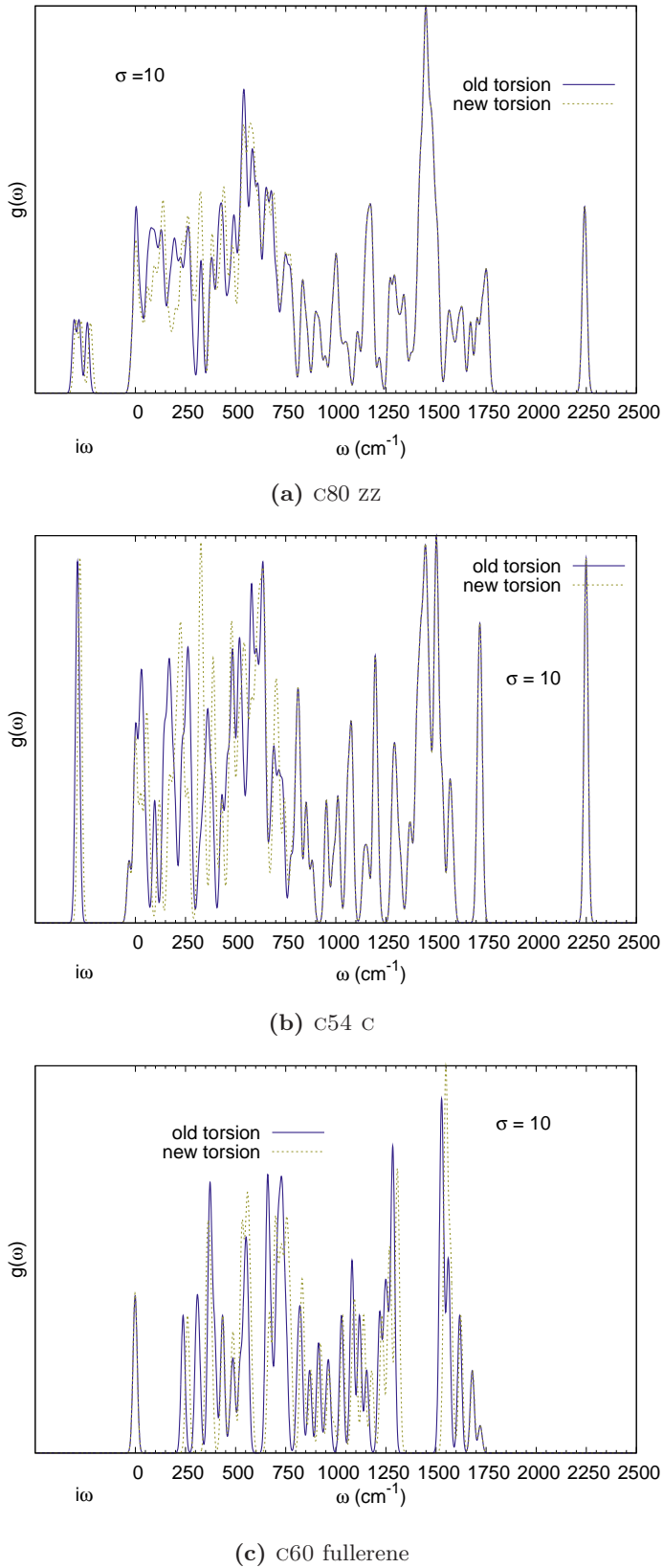


Figure 5.5: Phonon DOS for the old (solid blue) and new (dotted green) torsion term in LCBOPII; (a) C80 zz, (b) C54 c, (c) C60. All samples were equilibrated at 0.01K and the DOS was constructed with $\sigma = 10$. The low frequency modes (out of plane) shift to higher frequencies whereas the high ω modes are not affected. For (c) the new torsion changes the DOS slightly for all ω .

5.2.2 Comparison of DOS to single configurations

To calculate the DOS of a system at a certain temperature, we perform MC simulations in the canonical ensemble. The simulations provide us with a set of configurations that can be used to calculate averages in this ensemble. These configurations can then be fed to the phonon calculating code to get a DOS. At very low temperature, the differences in the possible configurations of our system are small and thus different realisations from our simulation yield almost the same DOS. When we increase temperature, the atoms start to move more out of their minimum-energy positions and the number of possible realisations gets larger. This is translated in noticeable differences in the resulting DOS. To get an idea about the “proper” shape of the DOS and since we are mainly interested in general features, we average the DOS calculated for many configurations. This section deals with the quality of these averages.

We equilibrated the C80 AC sample with a 10 Kelvin heat bath and calculated the DOS. Results of two consecutive configurations, together with their average is shown in figure 5.6.

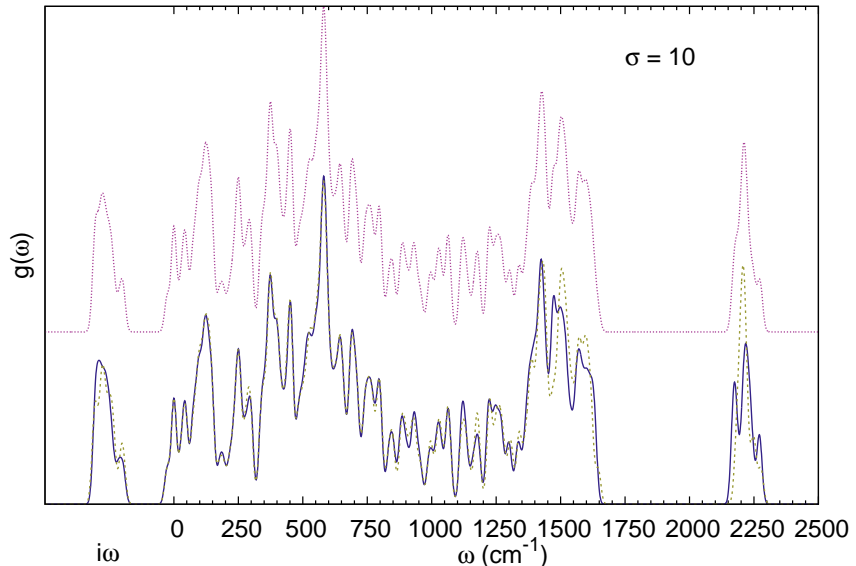


Figure 5.6: Phonon DOS ($\sigma = 10$) for two consecutive configurations (solid blue and dotted green) and the average (dotted purple) of these two DOS in a 10 Kelvin simulation. The curve of the averaged DOS shifted vertically to help comparison.

The peaks at $\omega \approx 1500 \text{ cm}^{-1}$ are globally reproduced for both frames but details of the spikes differ. This is even more apparent for the $\omega \approx 2200 \text{ cm}^{-1}$ structure. The average respects the overall structure but filters out the little differences.

In figure 5.7 we have plotted the average DOS when taking more and more frames into account. We see the averages smooth out the data but keep showing the main peaks. When the number of configurations used in the average increases, the DOS remains the same. In the following work, all presented DOS are averaged over multiple configurations, typically fifty.

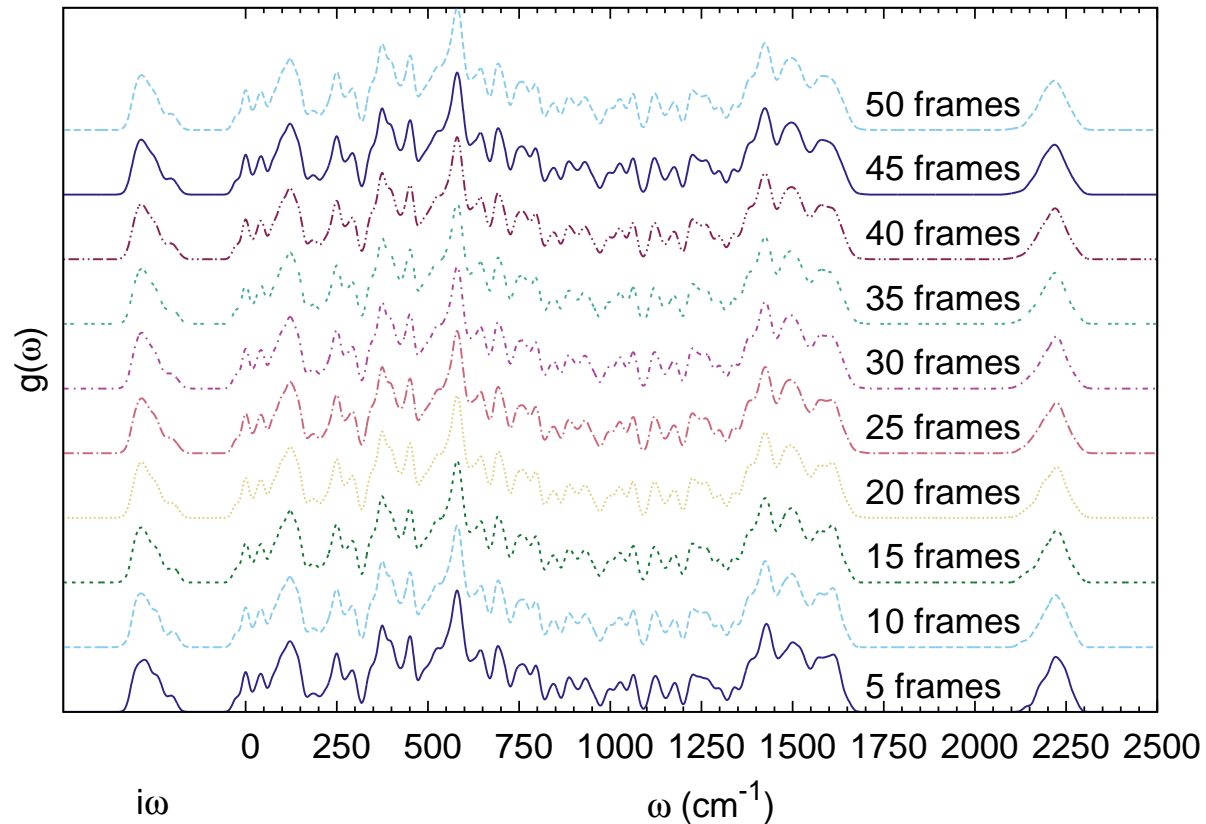


Figure 5.7: Phonon DOS ($\sigma = 10$) for averaged configurations in a 10 Kelvin simulation of c80 AC. The lowest line represents the DOS averaged over 5 configurations. Every higher line has 5 more configurations in the average. The averaged DOS shows all important structures.

5.2.3 Finite samples and finite temperature

The calculation presented in section 5.1 was performed for a periodically repeated unit cell where the results are meant to represent an infinite lattice. We can easily use the same procedure for the systems in which we are interested, like finite graphene flakes of different shapes and with different edges. The periodicity was ensured by defining a unit cell with label 1 that was repeated many times. If we want to study a finite system we can expand the unit cell to include the whole sample.

We construct initial samples that, either due to curvature or edges, are not automatically in the energy minimum of LCBOPII if the interatomic distance is taken to be that of graphite. To find the equilibrium configuration, we heated the samples to room temperature and then slowly cooled them down. For a few temperatures we simulated at constant temperature to ensure equilibration. Figure 5.8 shows details of this procedure applied to a C₆₀ fullerene. After this operation the structure is fully relaxed. We will call this procedure a Thermodynamical Equilibration Sweep (TES). If the bonds of this structure are subsequently stretched or compressed, a new TES brings the system back to the minimised configuration.

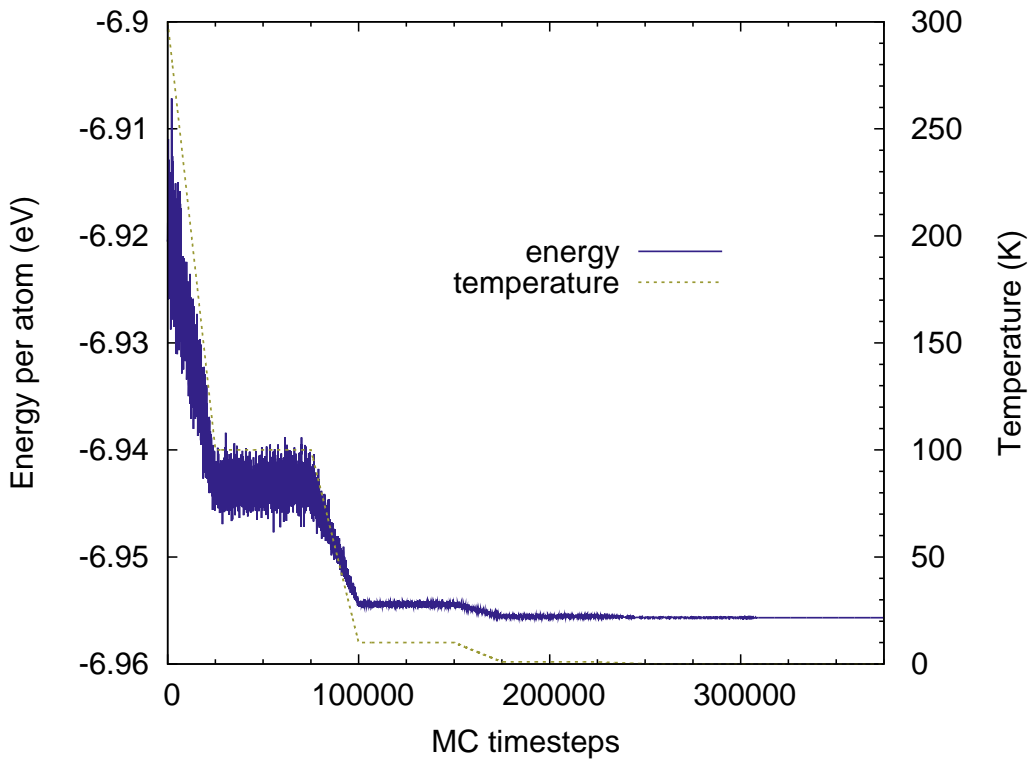


Figure 5.8: Energy (solid blue) and temperature (dotted green) for the TES of a C₆₀ molecule. The molecule started at 300 Kelvin and was subsequently cooled to 0.01 Kelvin. The plateaus where the temperature was constant can be seen.

In figure 5.9 we compare the phonon DOS of two finite systems minimised in a TES to 0.01 Kelvin. The DOS of bulk graphene is plotted for reference. Both finite samples show high frequencies $\omega > 1575 \text{ cm}^{-1}$ that are absent in the bulk graphene. The peaks at $\omega = 0 \text{ cm}^{-1}$ are explained by the translational and rotational invariance. The most apparent difference between the c80 AC and the fullerene system are the two gaps in the spectrum of the latter at $\omega \approx 610 \text{ cm}^{-1}$ and 1350 cm^{-1} . Furthermore, the c80 AC sample shows some very stiff modes of $\omega > 2200 \text{ cm}^{-1}$ and has modes with imaginary frequencies. The following section deals with the interpretation of these modes.

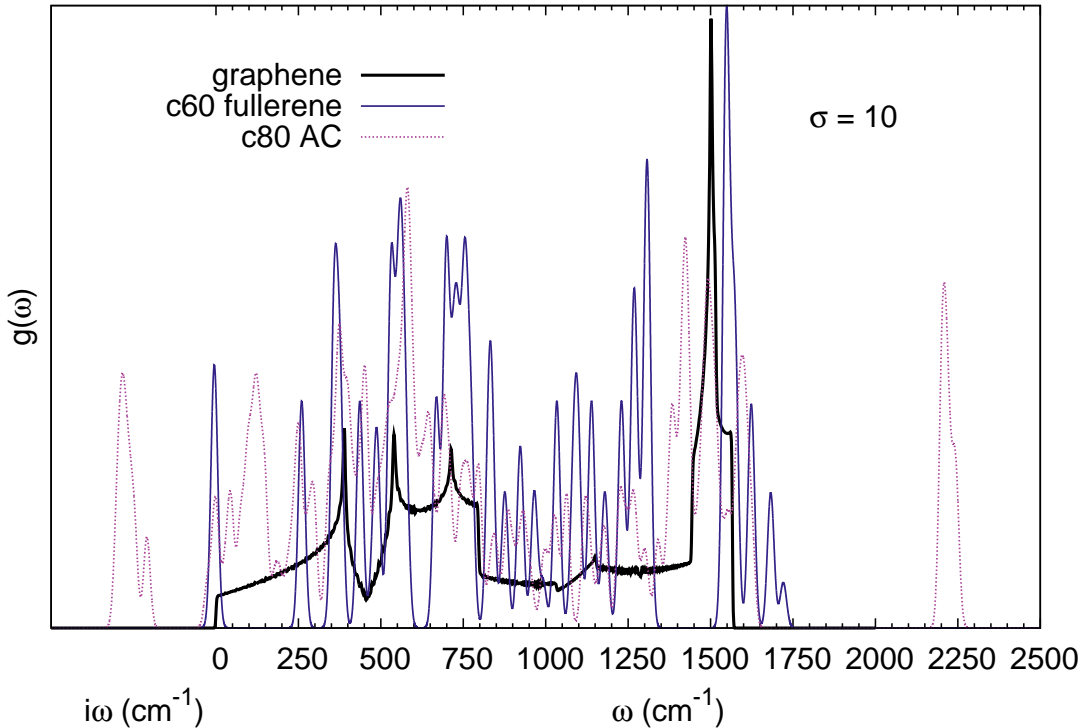


Figure 5.9: Phonon DOS ($\sigma = 10$) for bulk graphene (solid black), a c60 fullerene (solid blue) and a c80 AC flake (dotted purple). The DOS of the graphene has been scaled down to fit the plot. The finite samples are configurations from a TES to 0.01 Kelvin. Some of the peaks of the bulk are still recognisable in the finite samples e.g. $\omega = 390 \text{ cm}^{-1}$ and $\omega = 535 \text{ cm}^{-1}$. The c80 AC system shows imaginary modes, indicating an unstable configuration.

5.2.4 Imaginary modes

The occurrence of the imaginary frequency modes in the DOS of the c80 AC sample suggests that the sample is unstable. Since the atomic displacements calculated by equation 5.8 scale with $\exp(-i\omega t)$, an imaginary frequency makes the amplitude divergent. To study the effect of such a mode on the sample we have calculated the energy of the configuration when we displace the atoms by the eigenvectors corresponding to the $\omega = 300i \text{ cm}^{-1}$ mode. The results are shown in figure 5.10. For small amplitudes the energy of the system decreases.

This phonon mode moves the atoms of the sample to a position with a lower energy so we conclude that the configuration that was used to calculate the phonon frequencies was not at the energy minimum of the potential. There is a mismatch between the energy of the TES simulation that we used to equilibrate the sample at a certain temperature and the one given by the potential used to calculate the phonons.

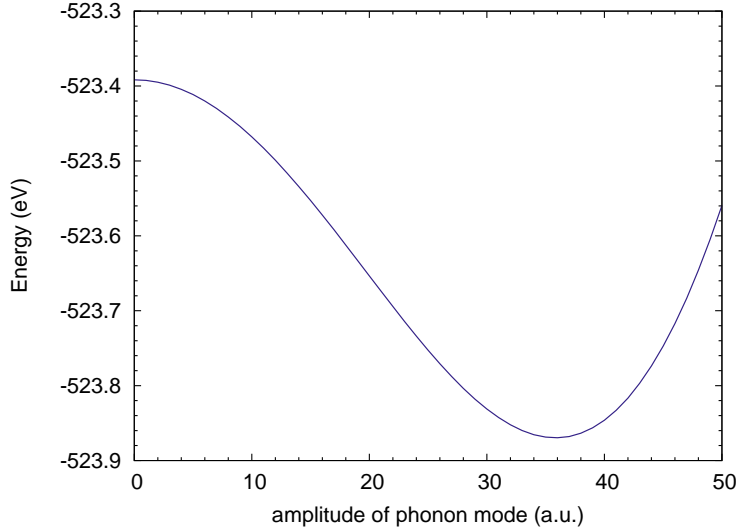


Figure 5.10: Energy of the C80 AC sample when its atoms are displaced by the eigenvectors of one of the imaginary modes. Since the energy decreases the initial sample was not a minimum energy configuration.

We can identify this difference in the energy. The potential in the phonon calculation code has no implementation of the edge reconstruction algorithm introduced in section 2.1.1. Thus the configuration with lowest energy in the TES simulation is not in the minimum energy state of the phonon calculation potential. The energy mismatch for the C54 C flake is presented in table 5.1 to illustrate this point.

Energy per atom (eV)	without edge reconstruction	with edge reconstruction
TES	-6.56983	-6.70860
phonon calculation	-6.56983	-6.55057

Table 5.1: Energies of the TES simulations and the phonon calculation simulations for a circular c54 C sample at 0.01 Kelvin. The columns show the inclusion of the edge algorithm in the TES simulations. If this is switched off, the phonon code gives the same energy per atom. Including the edge algorithm lowers the energy in the TES but results in a configuration that is not at a minimum energy configuration of the phonon calculation potential. The energy mismatch between the simulations is $\Delta E = 0.158$ eV per atom.

If the imaginary frequencies are due to the inclusion of the edge algorithm we can see if the phonon spectrum changes when we ignore this term. In figure 5.11 we present the DOS of the C80 AC flake produced in a TES with the edge algorithm switched on and off. When we minimise the sample without the edge algorithm we do not find imaginary modes in the DOS and the modes at $\omega \approx 2200\text{ cm}^{-1}$ shifts to lower frequencies.

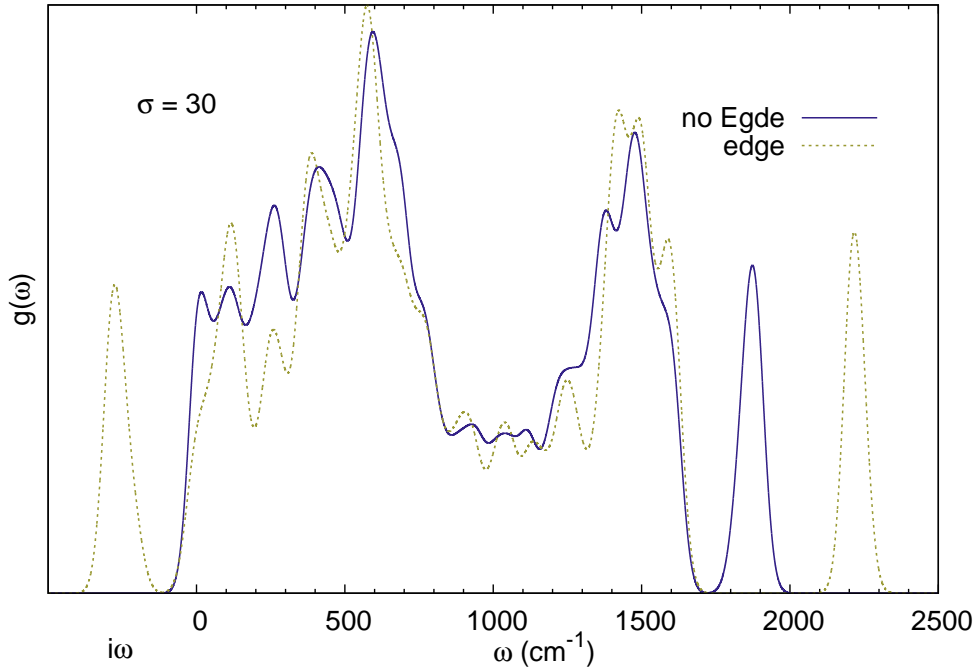


Figure 5.11: Phonon DOS ($\sigma = 30$) for the C80 AC sample. The solid blue line shows the DOS for the minimal energy configuration in a simulation with the edge algorithm switched off. The dotted green line shows the DOS when the sample was equilibrated in a TES where the edge algorithm was active and the phonons were calculated without this algorithm. The imaginary frequencies only appear in the simulation that used the edge algorithm and the high ω modes are located at a higher frequency.

We compare the phonon modes of the spectra by looking at the amplitude of their eigenvectors. In figure 5.12 and 5.13 on pages 44 and 45 we show seven of the modes with imaginary frequency and the seven highest modes with $\omega \approx 2220\text{ cm}^{-1}$. In figure 5.14 on page 46 we show the seven highest modes for the configuration equilibrated without the edge algorithm. All modes depicted are localised on the edge of the sample. The modes with imaginary frequency are z modes, moving perpendicular to the sample. They are not present in the DOS of the configuration that is in the energy minimum of the phonon calculation potential. The modes at high frequency move primarily in the xy plane. When calculated for a configuration produced with the edge algorithm switched on, they have the same character as the $\omega \approx 1850\text{ cm}^{-1}$ modes of the configuration that was in the energy minimum of the phonon code potential. The code that calculated the phonons overestimates the frequency of the edge modes when the sample is not in its potential minimum.

The inclusion of the edge reconstruction algorithm in LCBOP II changes the minimum energy configuration. Since the phonon code does not include this term in its potential, an energy mismatch between the two is expected. This leads to imaginary modes in the phonon DOS and an overestimation of the frequency of localised edge modes. The C₆₀ fullerene does not have modes with these frequencies since it has no edges and the results do not depend on the edge reconstruction algorithm.

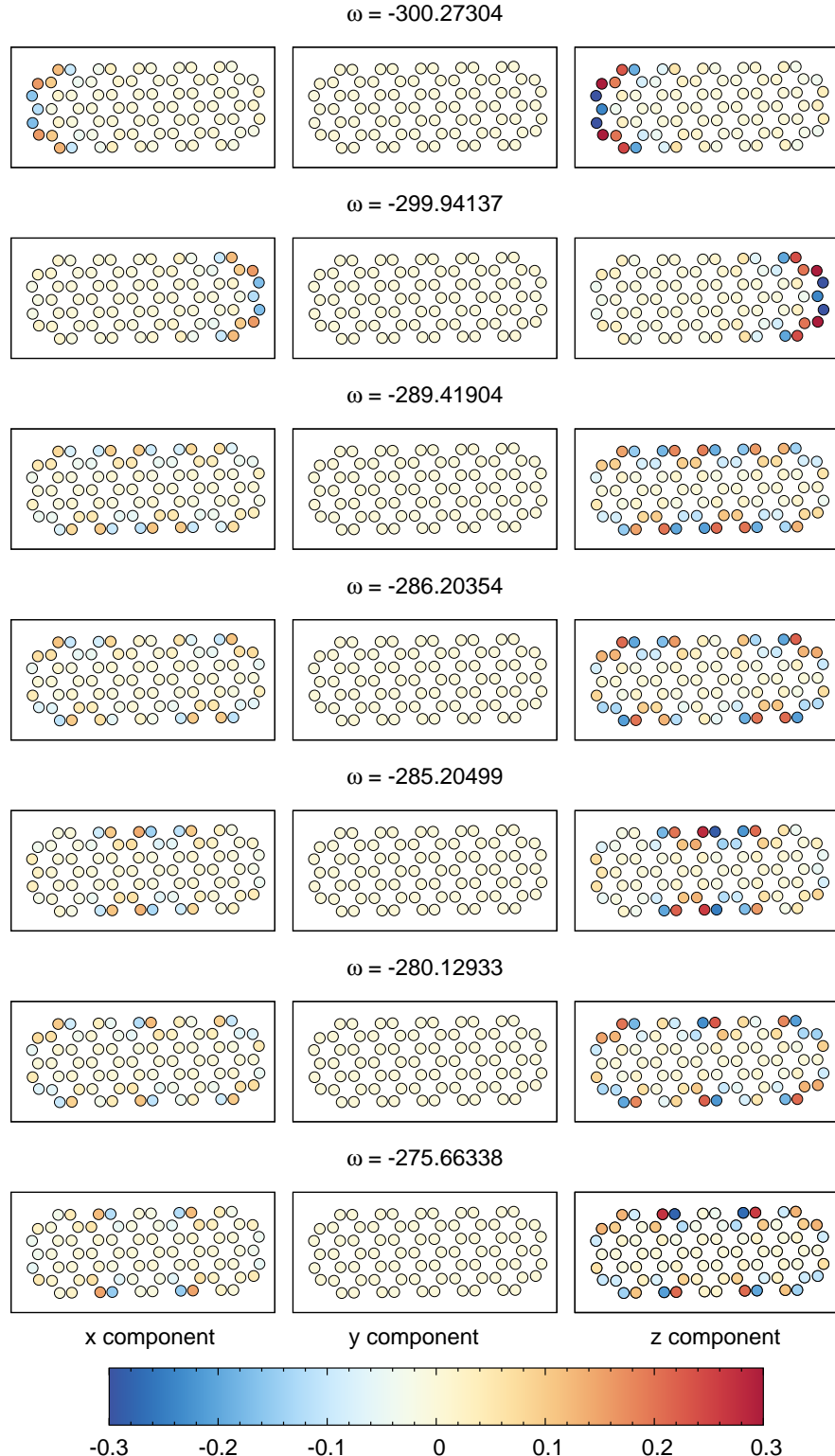


Figure 5.12: Amplitudes of the eigenvalues for seven of the imaginary frequency modes of the c80 AC sample equilibrated in a TES with the edge algorithm switched on. Left column: x component, middle column: y component and right column: z component. The frequency of every mode is printed above, the negative sign indicates an imaginary mode. Every circle represents an atom, the colour coding gives the amplitude of the component at that atom. All modes are localised at the edge of the sample and have large z components.

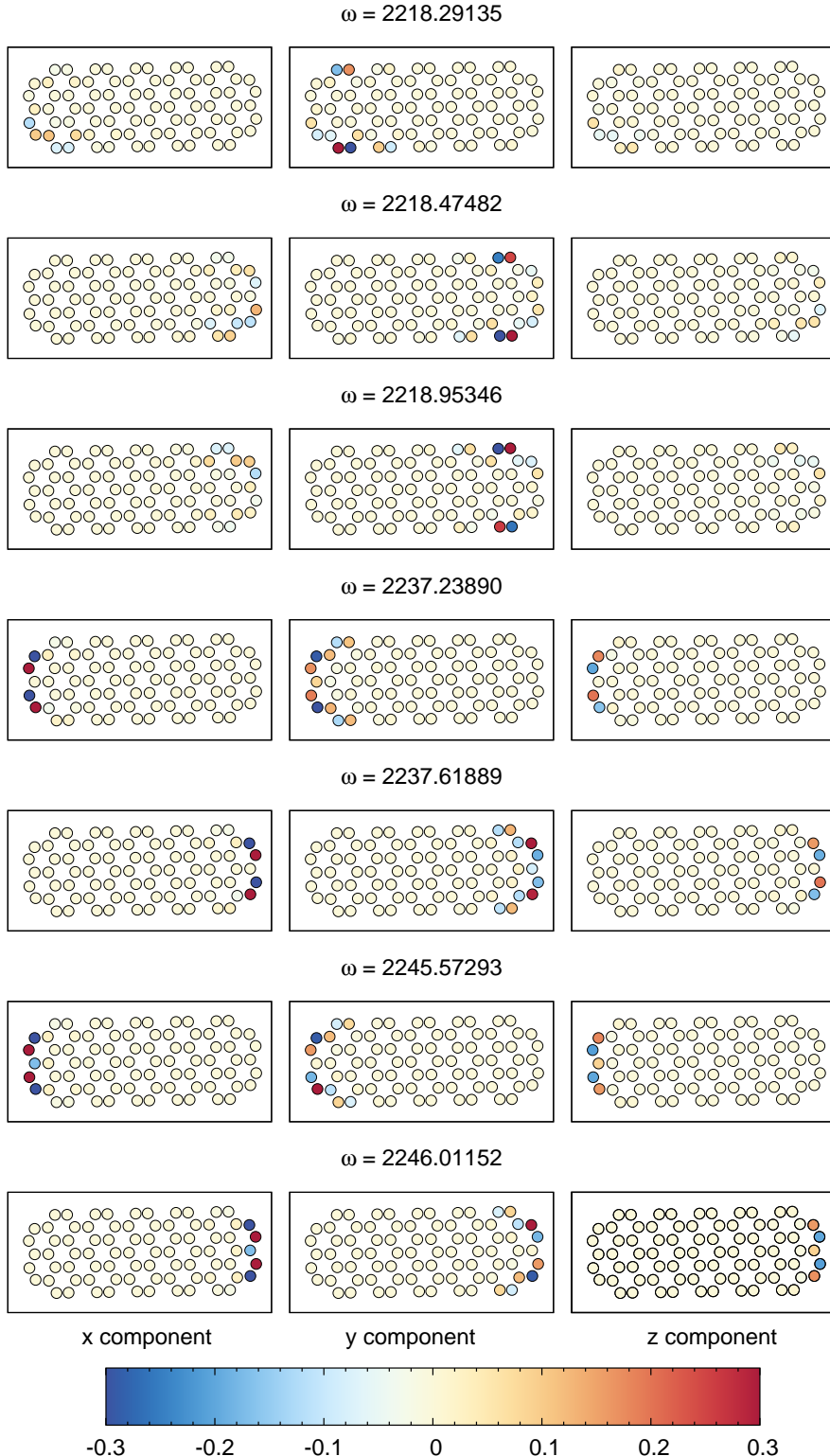


Figure 5.13: Amplitudes of the eigenvalues for the seven highest frequency modes of the C80 AC sample equilibrated in a TES with the edge algorithm switched on. Left column: x component, middle column: y component and right column: z component. The frequency of every mode is printed above. Every circle represents an atom, the colour coding gives the amplitude of the component at that atom. The first four depicted modes are in plane whereas the last three have a nonzero z component. All modes are localised at the edge of the sample.

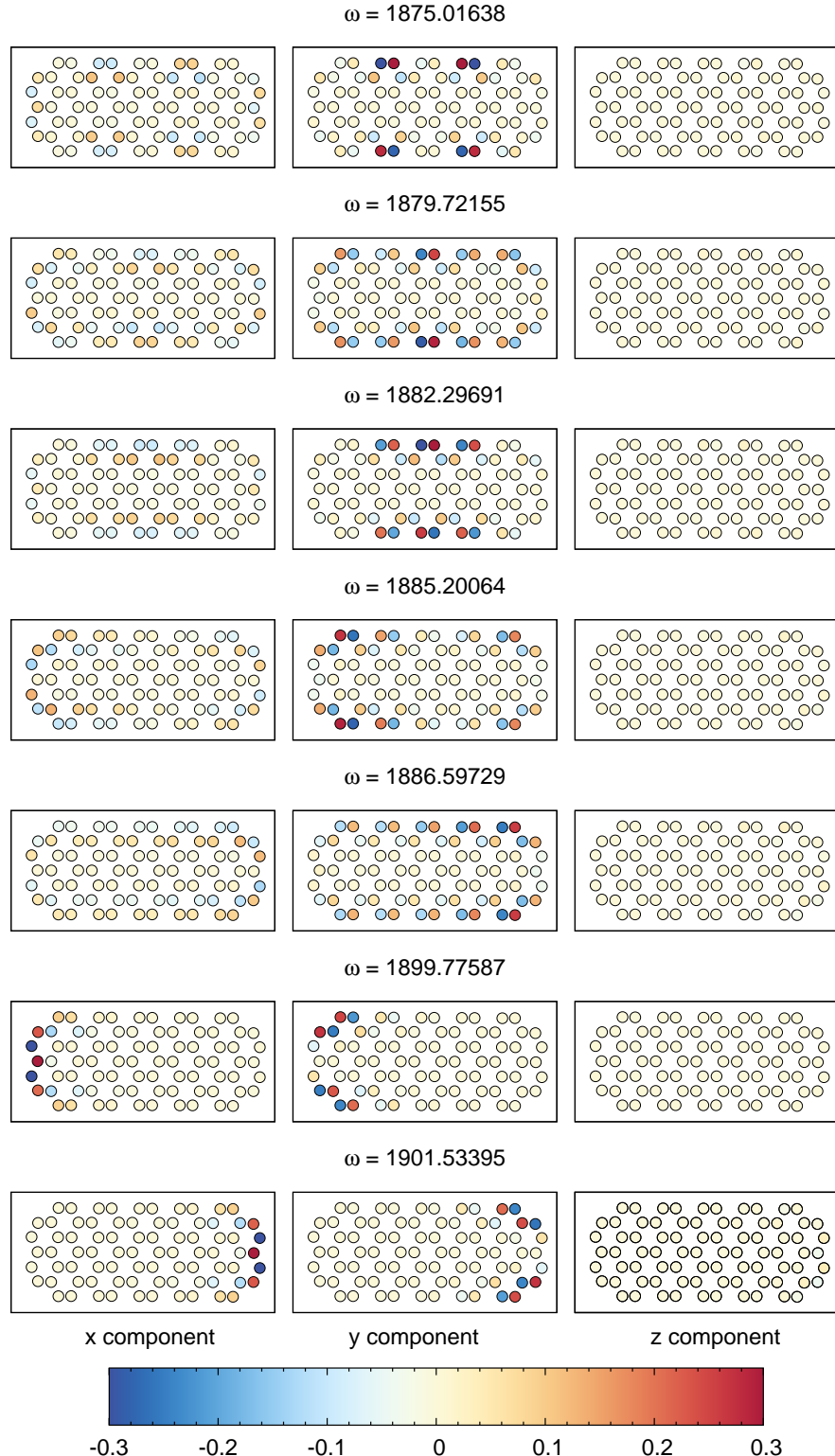


Figure 5.14: Amplitudes of the eigenvalues for seven of the high frequency modes for the c80 AC sample equilibrated in a TES with the edge algorithm switched off. Left column: x component, middle column: y component and right column: z component. The frequency of every mode is printed above. Every circle represents an atom, the colour coding gives the amplitude of the component at that atom.

5.2.5 Comparison of the calculated DOS with experiment

To get an impression of the quality of our calculated spectra we compare the calculated DOS of C₆₀ with experimental results presented by Menendez and Page [26]. The results are shown in figure 5.15. Four IR active modes and ten Raman active modes, calculated with DFT by Schettino et al. [29], are indicated by the vertical lines.

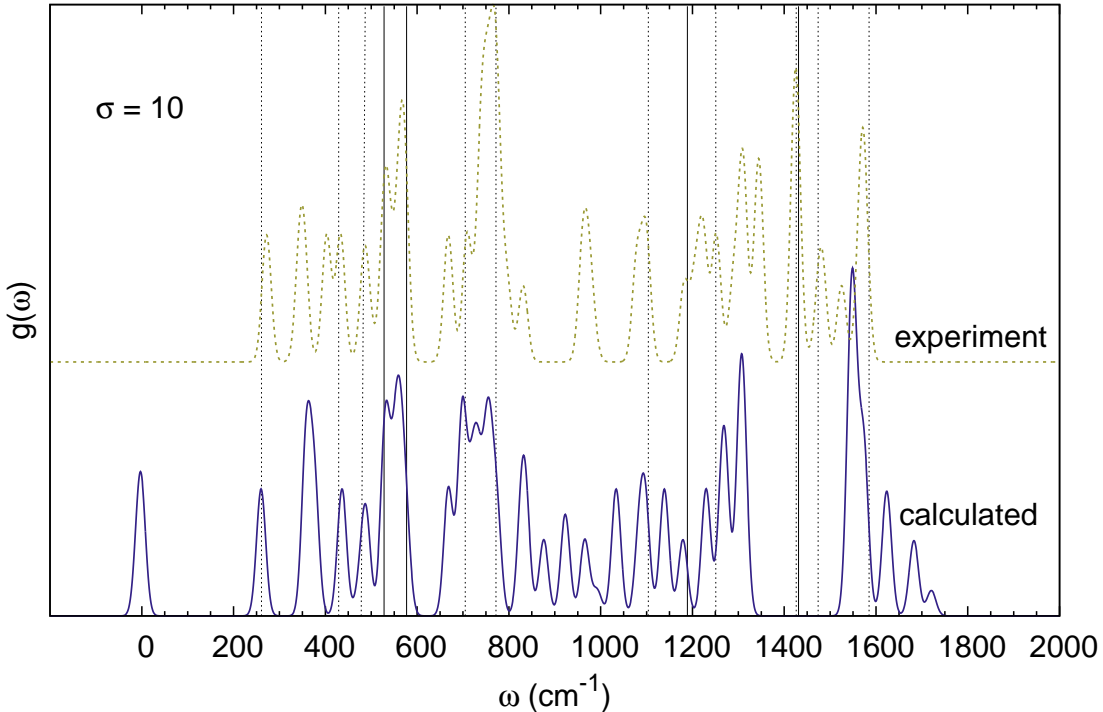


Figure 5.15: Phonon DOS ($\sigma = 10$) of the C₆₀ fullerene molecule. Results of our calculation at 0.01 Kelvin (solid blue) and experimental data (dotted green) from [26]. The vertical lines show the IR active modes (solid black) and the Raman active modes (dotted grey) as found in DFT calculations [29].

The two spectra are very similar at frequencies below 850 cm⁻¹. Furthermore, the fourteen active modes are almost all visible in the calculated DOS. The two fingerprint frequencies of chapter 3, $\omega = 527 \text{ cm}^{-1}$ and $\omega = 571 \text{ cm}^{-1}$ are very well reproduced. However, there is a gap in the calculated spectrum at $1350 \text{ cm}^{-1} < \omega < 1500 \text{ cm}^{-1}$ and higher calculated frequencies do not seem to have a counterpart in the experimental DOS. Comparing the shape of the high-end parts of both DOS it could be that our code overestimates these frequencies. We have also seen high frequency modes for the finite samples that are not in the minimal energy configuration due to the application of the edge algorithm. However the high ω modes in C₆₀ are not explained by this energy difference; they are also found in configurations produced in a TES without the edge term in the potential.

5.2.6 Temperature effects of the phonon Density of States

It is expected that a finite temperature changes the DOS of the samples since it affects the spread of inter-atomic distances. Furthermore, temperature can also lead to local curvature of the sample as explained in chapter 4. To investigate the connection between temperature and the DOS we have looked at the C80 AC system at different temperatures. Results for the radial distribution function $g(r)$ and the phonons DOS are in figure 5.16 and 5.17 respectively.

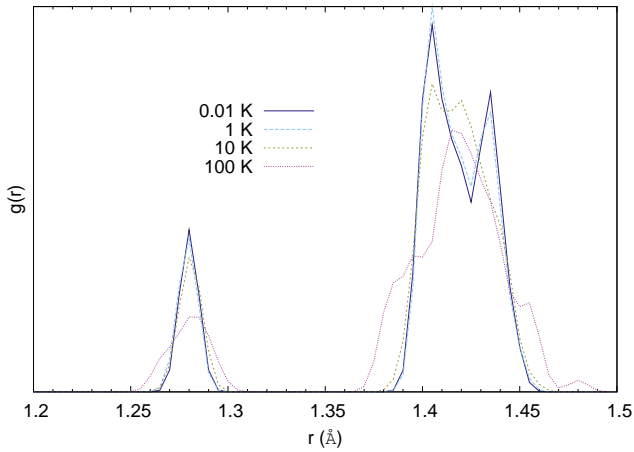


Figure 5.16: Radial distribution function for the C80 AC structure. T = 0.01 Kelvin (solid dark blue), 1 Kelvin (dotted light blue), 10 Kelvin (dotted green) and 100 Kelvin (solid purple). As expected, the temperature broadens the peaks.

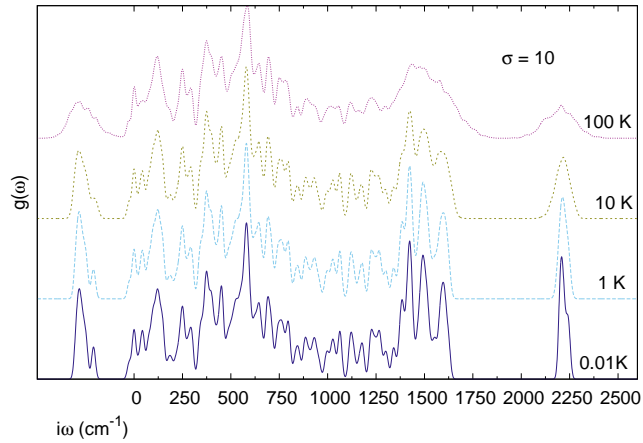


Figure 5.17: Phonon DOS ($\sigma = 10$) for C80 AC at different temperatures. As temperature increases, the peaks in the spectrum broaden but the overall features can still be distinguished.

The peaks in the radial distribution function and those in the DOS broaden as expected. However, the overall shape of the DOS remains the same and the peaks in the DOS can, at large, still be recognised at finite temperature.

5.3 The phonon spectrum and structural differences

We have seen how we can calculate the phonon DOS of finite samples and interpret the result. Now we are able to study the variations of the DOS of carbon systems in different configurations. We can vary the length and width of a sample but also the type of edge termination. Furthermore, we can study the impact of defects on the phonon spectrum. Does the DOS of such systems reflect the variation in structure and does curvature discussed in chapter 4 have any distinguishable effects?

5.3.1 Variations in carbon configuration

Length differences

In chapter 4 we looked at the temperature induced ring angle deficit for many different structures. One of the parameters that varied for the systems was their length. The c80 zz , c104 zz and c120 zz (see figure 4.11) flakes share their structural buildup as zigzag terminated ribbons with a three ring width but their length varied. In figure 5.18 we show the phonon DOS for these structures. As explained in section 5.1, the number of phonon modes (and hence the area under the DOS) is proportional to the number of particles, so to aid comparison we have scaled this curve.

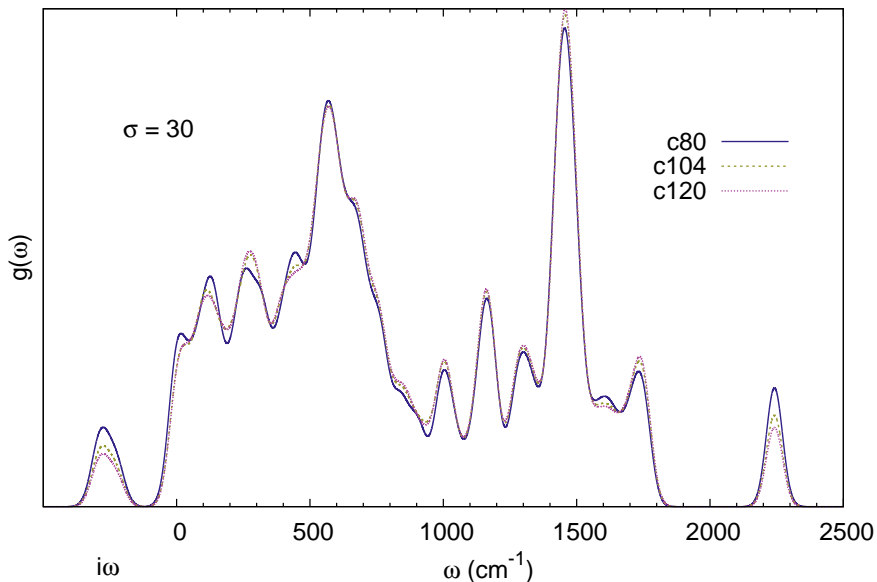


Figure 5.18: The phonon DOS ($\sigma = 30$) for the three zigzag terminated flakes shown in figure 4.11 with the same width but different length. The DOS has been scaled by the number of modes to aid comparison. The main differences occur at the unstable imaginary modes and the at the localised modes at $\omega > 2000 \text{ cm}^{-1}$.

The increased length of the samples does not change the phonon spectrum for the zz terminated structures. The main peaks have the same intensity and the overall shape of the spectrum is the same. However, the imaginary modes and localised modes at $\omega > 2000 \text{ cm}^{-1}$ change intensity. This is because the number of imaginary frequency modes and high ω modes do not change

for the structures. The modes are localised on the short (AC like) edge of the sample and that is constant in size. This means that the relative contribution of these modes decreases for a larger ZZ terminated flake.

In figure 5.19 we look at two armchair terminated flakes that share the same width. The first is the C80 AC system and for the second an extra row of carbon rings was added, creating the C104 AC flake (see appendix A for the structure). Both flakes have the same width of four and the length is eleven and seventeen respectively. Figure 5.19 shows the DOS of both samples.

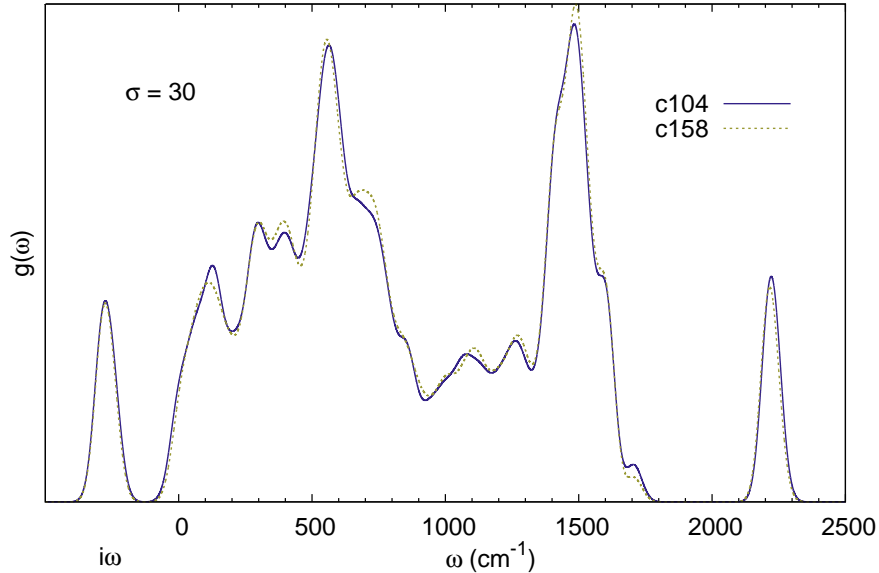


Figure 5.19: The phonon DOS ($\sigma = 30$) for two armchair terminated flakes shown in figure 4.11 with the same width but different length. The DOS has been scaled by the number of modes to aid comparison. Since the unstable imaginary modes and at the localised modes at $\omega > 2000\text{ cm}^{-1}$ are now of equal intensity. Because the modes are located at the long edge the possible number of modes grows with the length of the flake so the relative contribution stay the same for bigger samples.

Width variations

We can also vary the width of the samples. In figure 5.20 we look at three armchair terminated systems: C80 AC, C158 AC and C172 AC (shown in figure 4.11) with widths of three, four and five respectively. The lengths of these three flakes does differ (eleven, seventeen and fifteen) but we have seen that this does not influence the spectra. In figure 5.21 the DOS of two zigzag terminated flakes with the same length of 10 but different widths (three and five) is shown.

The width of a flake does have an effect on the DOS. The main peaks are discernible in all the presented structures but their relative intensities change. The smallest structure has a strong peak at $\omega \approx 1580\text{ cm}^{-1}$ and three distinct peaks at $1400\text{ cm}^{-1} \lesssim \omega \lesssim 1650\text{ cm}^{-1}$. In the larger structures the first peak loses intensity in favour of a mode at $\omega \approx 1750\text{ cm}^{-1}$. The three other peaks move closer together, creating one very strong frequency at $\omega \approx 1500\text{ cm}^{-1}$. This is a manifestation of spatial quantisation. Like with a one dimensional quantum well, when the systems becomes wider the energy gap between the states gets smaller. Thus, the peaks in the DOS move closer together.

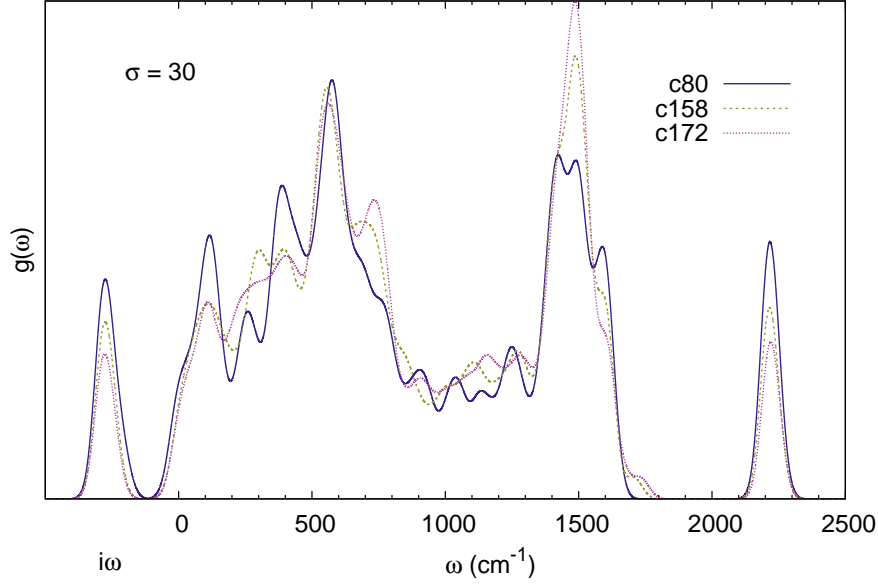


Figure 5.20: The phonon DOS ($\sigma = 30$) for three armchair terminated flakes. The DOS has been scaled by the number of modes to aid comparison. Although the same frequencies are strong in all flakes, their relative intensity differs. The three distinct modes in the c80 AC flake at $1400 \text{ cm}^{-1} \lesssim \omega \lesssim 1650 \text{ cm}^{-1}$ move closer together for the wider systems.

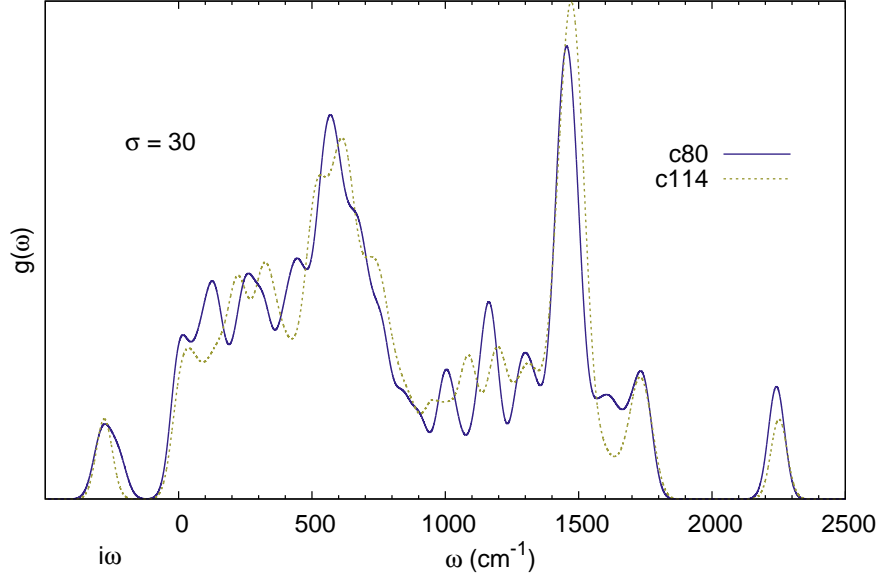


Figure 5.21: The phonon DOS ($\sigma = 30$) for two zigzag terminated flakes. The DOS has been scaled by the number of modes to aid comparison. Although the same frequencies are strong in all flakes, their relative intensity differs.

5.3.2 Edge termination differences

Another structural difference in the flakes that we have studied is the edge termination. The c80 AC and c80 zz flake share the same number of atoms and width but their edges are different. The average coordination number of the two structures is almost the same (2.625 for the AC structure and 2.65 for zz), but the c80 AC has one ring less. We have calculated the phonon spectra for configurations at 0.01 Kelvin. To aid comparison we show the resulting DOS in figure 5.22.

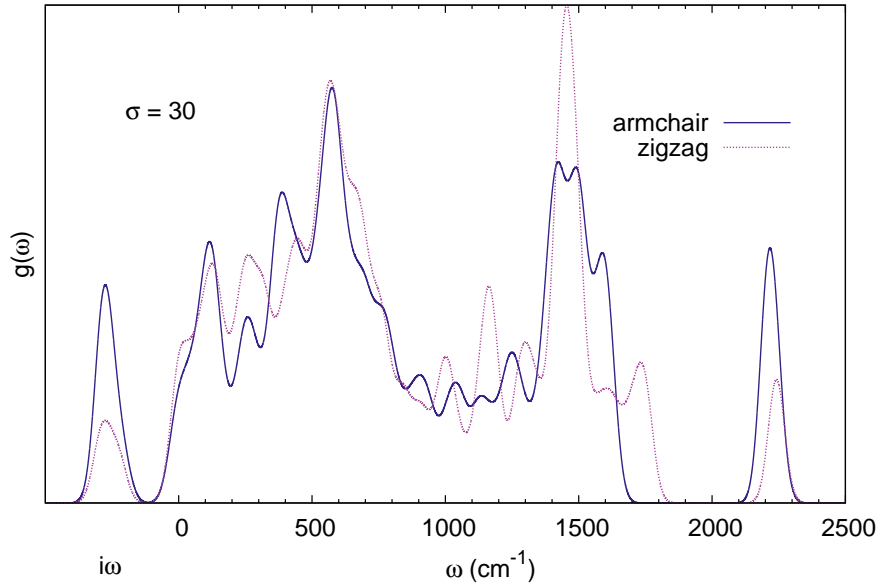


Figure 5.22: Phonon DOS ($\sigma = 30$) for c80 AC and c80 zz structures at 0.01 K. The edge type has profound effects on the phonon spectra.

We see some big differences between the two spectra. At $\omega \approx 1500 \text{ cm}^{-1}$ the zigzag terminated sample has a single shouldered peak whereas the armchair terminated structure shows three distinct modes. Another difference is the existence of modes between $1650 \text{ cm}^{-1} < \omega < 1800 \text{ cm}^{-1}$ for the zigzag sample. A third noticeable feature is the strong peak at $\omega \approx 1250 \text{ cm}^{-1}$ that is only visible in the spectrum of the zigzag terminated flake. The type of edge has a big influence on the phonon spectrum of a carbon flake.

5.3.3 Defects in the lattice

Edge reconstruction and Stone-Wales defects

As we have seen in 2.1.1, the zigzag edge of c80 zz is not the minimal energy state. An edge reconstruction to a 5-7 configuration (see figure 4.17) lowers the energy of the system. Such reconstructions change local interatomic distances and may influence the phonon dispersion. Another structural deformation of graphitic systems is the Stone-Wales (sw) rearrangement explained in section 4.6.

Figure 5.24 shows the DOS of a pristine C80 zz flake and two samples with these two possible defects. The 5-7 defected sample was prepared in a TES simulation to 0.01 Kelvin. The flake with the SW defect is shown in figure 5.23. It has a defect in the middle and is flat. This differs from the SW defected samples we studied earlier in section 4.6, which had curvature. The difference between the two flakes lies in the production scheme. When we minimise the structure in a TES we find the highly curved structure presented in 4.11 but when we simulate directly at 0.01 Kelvin, the flakes remains much flatter. Comparing the energies, we found that the curved structure has a lower energy, indicating that for good energy minimisation, the simulation pathway is very important.

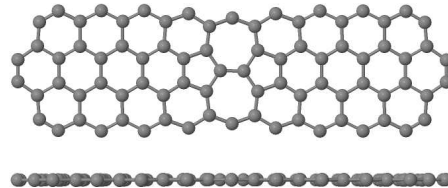


Figure 5.23: Top and side view of a C80 zz flake with a Stone-Wales defect in the middle. Note that this flat sample is not the lowest energy configuration of this system.

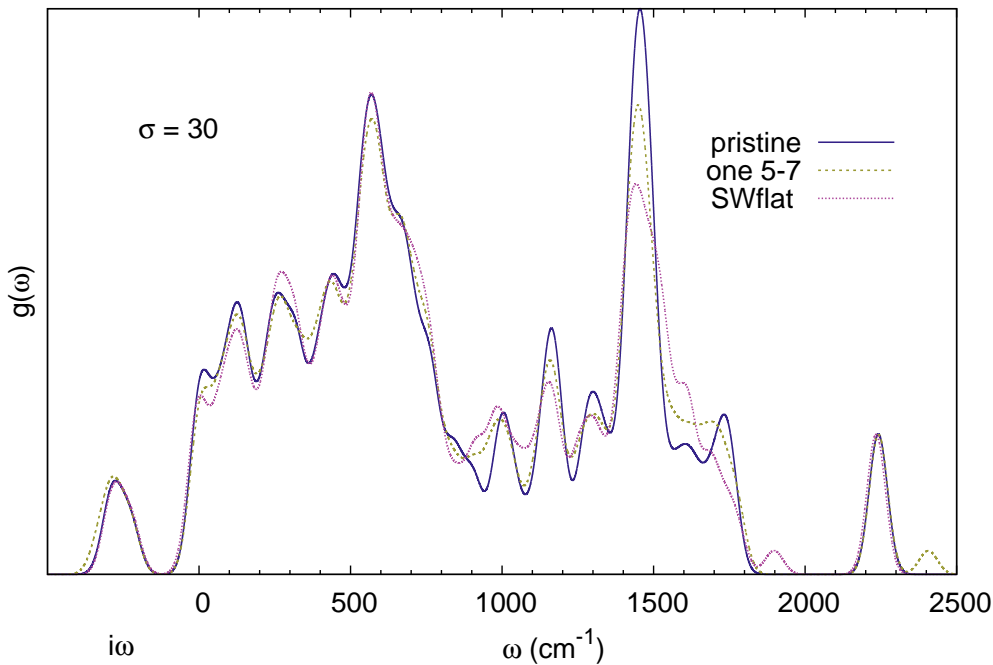


Figure 5.24: Phonon DOS ($\sigma = 30$) for a pristine C80 zz flake and two defected flakes at 0.01K. The defects lower the intensity of the $\omega \approx 1500 \text{ cm}^{-1}$ peak and enhance the modes at higher frequencies.

The defects in the lattice shift the modes at $\omega \approx 1500 \text{ cm}^{-1}$ to higher frequencies. Besides this, there is little effect of the defects on the DOS.

Defects of c60

The phonon spectrum of C₆₀ has been presented in earlier sections of this chapter. Although the DOS shows most of the active spectral lines, we found a large gap in the spectrum between $1350\text{ cm}^{-1} < \omega < 1500\text{ cm}^{-1}$ where our code does not reproduce experimental data. The gaps may be explained by the high symmetry of the molecule. We tested this idea by changing one of the vertices to form a square and two heptagons instead of a pentagon and two hexagons, creating C₆₀* as shown in figure 5.25. Figure 5.26 shows the DOS. The configurations were produced in a TES to 0.01 Kelvin.

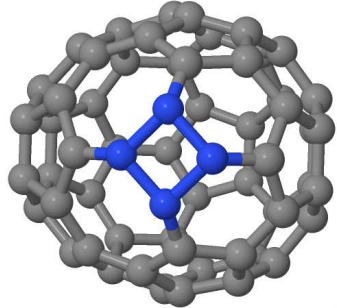


Figure 5.25: The defected C₆₀* structure. The created square has been labelled blue.

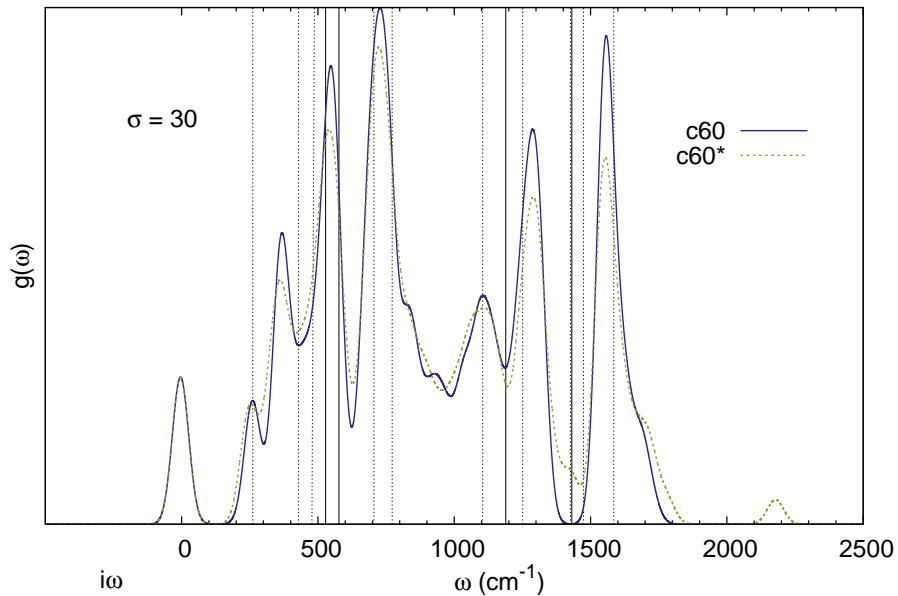


Figure 5.26: Phonon DOS ($\sigma = 30$) at 0.01K for relaxed C₆₀ and defected C₆₀*. Active IR (solid black) and Raman (dotted grey) modes are shown. The defect creates modes around $\omega \approx 1400\text{ cm}^{-1}$ and has localised modes with a high frequency.

The C₆₀* structure shows the missing modes at $\omega \approx 1400\text{ cm}^{-1}$. It also has a single high frequency mode at $\omega \approx 2180\text{ cm}^{-1}$ that is localised on the four atoms of the square. The slight increase in intensity at $\omega \approx 1780\text{ cm}^{-1}$ can also be related to localised modes on the defect.

5.3.4 Effects of curvature on the DOS

We have seen how differences in the configuration of the atoms in a sample affect the DOS. Now we focus on how curvature in a system manifests itself in the DOS. We first look at the c80 zz flake with a Stone-Wales defect in the middle. Figure 5.27 shows the DOS for the flat SW sample and the curved sample that we presented in section 4.6.

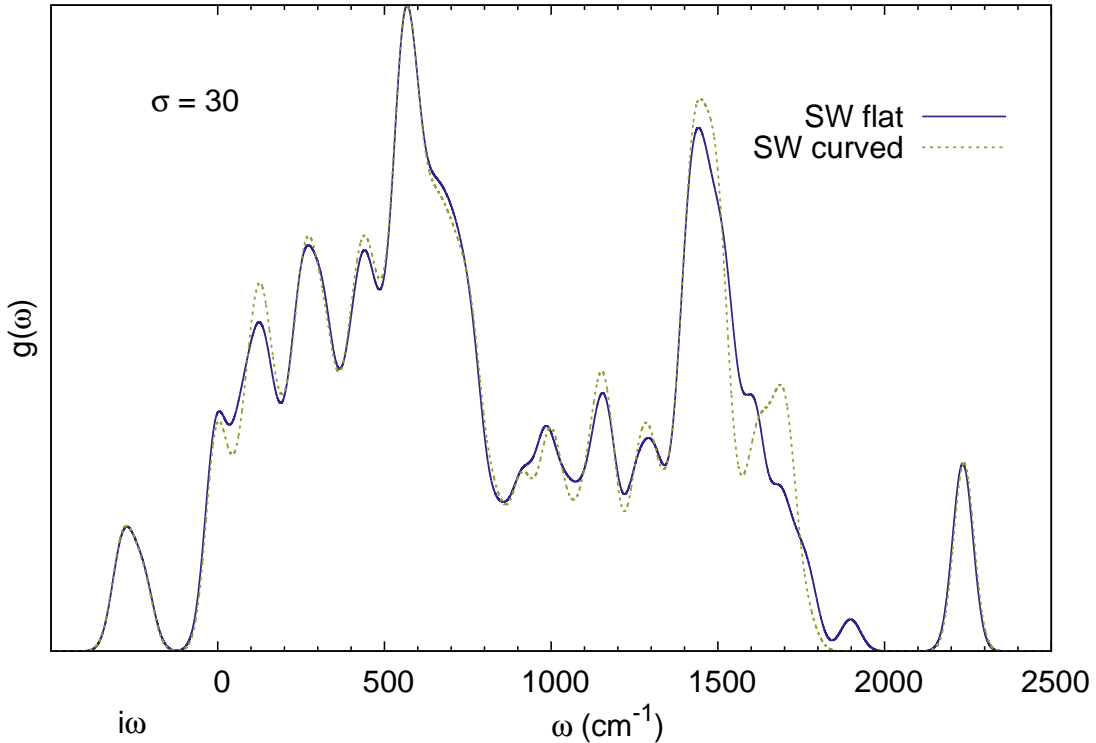


Figure 5.27: Phonon DOS ($\sigma = 30$) for the c80 zz flake with a Stone-Wales defect in the middle. The DOS of the flat configuration as well as the DOS of the curved configuration are shown. The main difference is seen at the modes with $\omega \approx 1700 \text{ cm}^{-1}$.

We see that the curvature does not change the spectrum for most of the frequencies. Only at the high frequency part $\omega > 1500 \text{ cm}^{-1}$ there is some clear difference. The curved sample has a strong peak at $\omega \approx 1700 \text{ cm}^{-1}$ whereas the flat sample has one peak near $\omega \approx 1600 \text{ cm}^{-1}$ and a single mode at $\omega \approx 1900 \text{ cm}^{-1}$. The latter is a mode localised on the defect. This mode is also present in the curved sample but at a lower frequency of $\omega \approx 1765 \text{ cm}^{-1}$. This is also true for the modes at $\omega \approx 1600 \text{ cm}^{-1}$. These modes are localised on the short edges of the sample and exist in the curved sample at $\omega \approx 1550 \text{ cm}^{-1}$.

Transition from a flat to a curved system

In section 4.5 we presented a graphene flake that formed a bowl as a result of induced curvature by pentagon formation. The general scheme of the process is shown in figure 5.28.

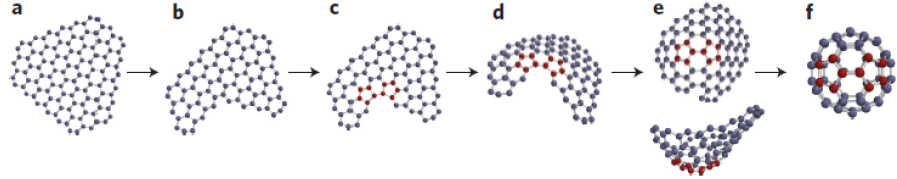


Figure 5.28: The carbon flakes from Chuvalin et al. [6]. From left to right we see the transition of a flat sample **a** to a fullerene **f** in a number of stages. We studied the curvature of these flakes in section 4.5.

Flake **c** and **d** are two snapshots with the same structure but different curvature. Averaging the ring angle deficit over the whole sample gives $\vartheta_r = 1.23^\circ$ per ring for **c** and $\vartheta_r = 1.38^\circ$ per ring for **d**. Figure 5.29 shows the DOS for the two samples.

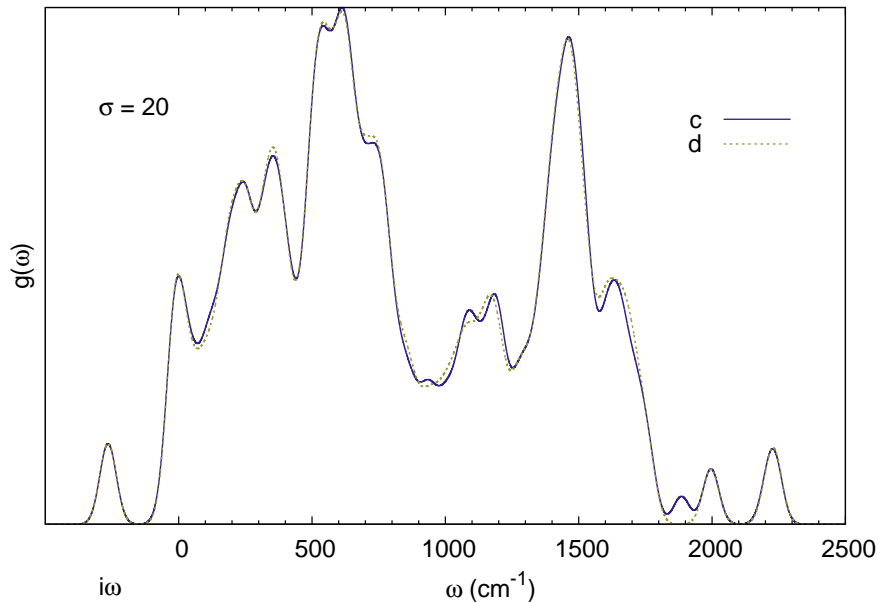


Figure 5.29: Phonon DOS ($\sigma = 20$) of **c** and **d** from 5.28. The flakes can be found in appendix A on page 59. The curvature has not a big influence on the DOS.

The DOS for the two sample is almost identical. Flake **c** has a single mode at $\omega \approx 1880 \text{ cm}^{-1}$. A corresponding mode cannot easily be identified in **d**.

The phonon DOS does not react strongly to changes in the configuration due to defects or to curvature. The main features of the spectrum are defined by the global structure of the system like the type of edge termination or size.

Chapter 6

Summary and discussion

The formation of large closed carbon systems in space is an active and interesting topic in science. There is proof that these systems are formed in the hydrogen deprived star envelopes via aggregation of small carbon clusters. We were able to reproduce this aggregation result by numerical MC simulation of a dense carbon gas in an box with periodic boundary conditions. However, when we used the edge reconstruction algorithm the yield of closed systems was significantly less. This has to do with the reduced reactivity of the edge of carbon flakes since the edge algorithm created stronger bonds between the edge atoms. The yield of closed systems by aggregation is thus limited by the self-passivating nature of the edge. Because of the discovery of fullerenes in parts of the tenuous interstellar medium, a second formation pathway has been proposed. In the new top-down route Polycyclic Aromatic Hydrocarbons (PAH) are subject to hydrogen and carbon loss due to bombardment with intense radiation. When a carbon atom at the edge of a dehydrogenated PAH is removed a pentagon will be formed. This induced local curvature. More pentagons will eventually lead to a globally curved system which zips up when the edges meet. The formed carbon cages then isomerise into fullerenes.

In order to study this phenomenon, we have defined two methods to analyse the curvature on a lattice. The vertex angle deficit ϑ_v and the ring angle deficit ϑ_r use the changing angles in a curving flake to classify the extent of the curvature. The ring angle deficit performs better. It naturally gives zero curvature for a flat flakes at zero temperature and increases linearly when the sample is heated. The factor of proportionality between curvature and temperature is dependent on the edge termination of the flake. We were able to quantify and visualise the induced curvature of pentagons in a graphene flake and describe the way the curvature is distributed over the samples. The pentagons themselves remain flat whereas the adjacent hexagons provide the angle deficit i.e. curvature.

It is still unclear if the top-down formation pathway of fullerenes has a high enough yield to account for the observed abundances. Since the atom loss due to radiation can create curvature in the wrong direction, there is only a limited range of flakes that can reach a size that enables it to follow a thermodynamically driven transformation into a fullerene. If the flake is too big the edges will not meet and zipping cannot occur; if the flake is too small the strain on the C – C bonds will become too large to make the route to a closed system energetically feasible.

Another problem with the proposed pathway lies in the supposed mobility of the pentagons. Only pentagons that are near the centre of a flake can induce global curvature. However, in the proposed mechanism the pentagons are formed at the edge of the sample. This means that there must be an efficient process where the edge pentagons migrate to the centre. Both Berné and Tielens [2] and Chuvalin et al. [6] mention such a mechanism but do not elaborate on its rate or efficiency. Although not thoroughly studied we have not seen any migration of the edge pentagons at the temperatures in which the top-down pathway is the main route to fullerene formation.

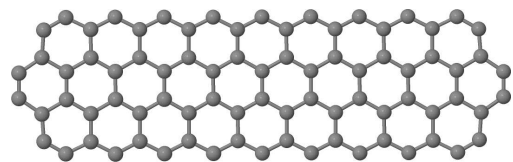
Since the astrophysical carbon species are detected by their infrared emissions, we calculated the phonon spectra for many different samples. We were able to reproduce many features of an experimental spectrum of the C₆₀ fullerene and we able to identify some of the infrared active modes.

Because of a mismatch between the potential used in the calculation of the phonons and the code used for thermal equilibration we found imaginary phonon modes and modes at very high frequency with similar eigenvectors. These modes were all localised on the edge of the sample. The imaginary modes lowered the energy of the sample, indication an energy mismatch between the used potentials. The difference in the potential lies in the inclusion of the edge reconstruction algorithm. When we did not include this term in the simulations we found only real frequencies and the high ω modes shifted to lower frequencies.

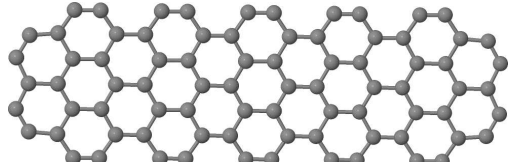
We studied the relation between the shape of a sample and its phonon spectrum. The phonon DOS is dependent on structural features of a sample like its size and edge termination. When the sample is small in a certain direction the effect of size quantisation can be seen. However, defects and curvature do not change the DOS of a sample in a considerable way. The modes at $\omega > 1500$ have some response but these effects are small and can also be related to the energy differences between the curved and flat samples.

Appendix A

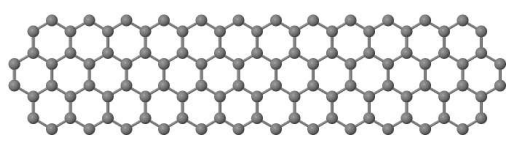
List of structures



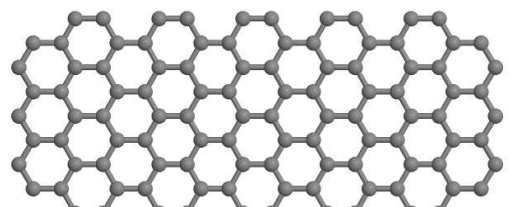
(a) c80 zz



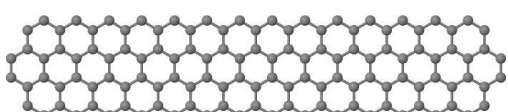
(b) c80 AC



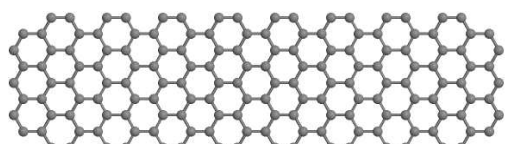
(c) c104 zz



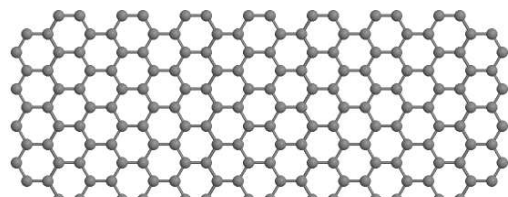
(d) c104 AC



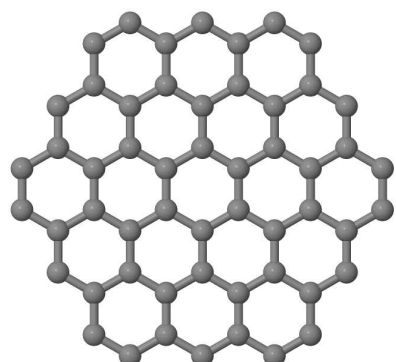
(e) c120 zz



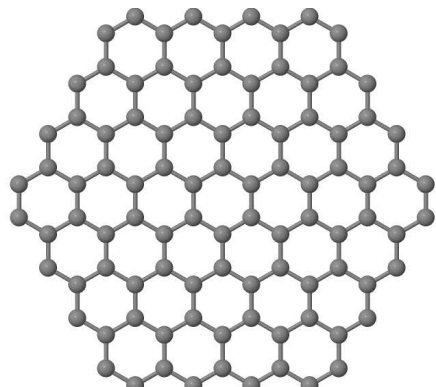
(f) c158 AC



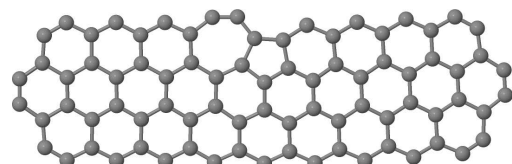
(g) c172 AC



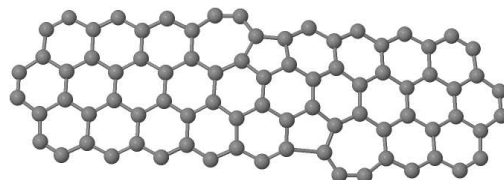
(h) c54 c



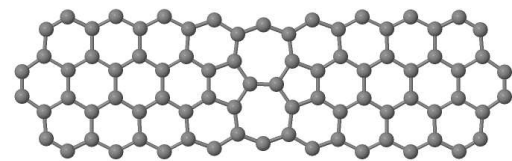
(i) c96 c



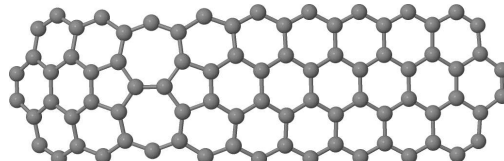
(j) c80 zz with one edge reconstruction



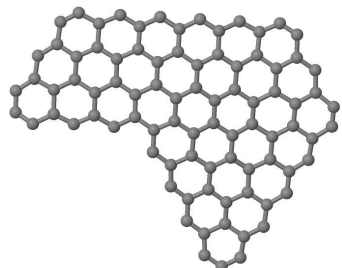
(k) c80 zz with two edge reconstructions



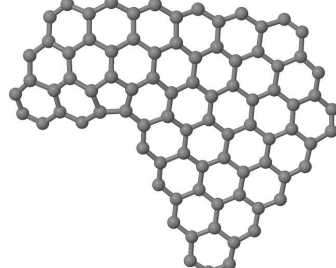
(l) c80 zz with a Stone-Wales defect at the center of the flake; flat configuration.



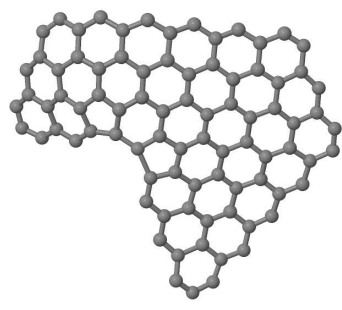
(m) c80 zz with a Stone-Wales defect at the side of the flake; curved configuration.



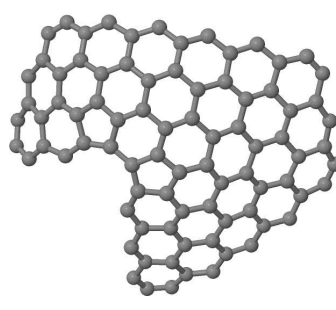
(n) flake b



(o) flake b'



(p) flake c



(q) flake d

Bibliography

- [1] M. A. Akhukov, A. Fasolino, and J. H. Los. Torsional barrier for graphitic bond. Private communication, October 2010.
- [2] O. Berné and A.G.G.M. Tielens. Formation of buckminsterfullerene (c60) in interstellar space. *Proceedings of the National Academy of Sciences*, 109(2):401–406, 2012.
- [3] D. W. Brenner. Empirical potential for hydrocarbons for use in simulating the chemical vapor deposition of diamond films. *Phys. Rev. B*, 42:9458–9471, Nov 1990.
- [4] J. Cami, J. Bernard-Salas, E. Peeters, and S. E. Malek. Detection of c60 and c70 in a young planetary nebula. *Science*, 329(5996):1180–1182, 2010.
- [5] I. Cherchneff, Y.H. Le Teuff, P.M. Williams, and A.G.G.M. Tielens. Dust formation in carbon-rich wolf-rayet stars. i. chemistry of small carbon clusters and silicon species. *Astronomy and Astrophysics*, 357:572–580, 2000.
- [6] A. Chuvilin, U. Kaiser, E. Bichoutskaia, N. A. Besley, and A. N. Khlobystov. Direct transformation of graphene to fullerene. *Nature chemistry*, 2(6):450–453, 2010.
- [7] S. Fahy, Steven G. Louie, and Marvin L. Cohen. Pseudopotential total-energy study of the transition from rhombohedral graphite to diamond. *Phys. Rev. B*, 34:1191–1199, Jul 1986.
- [8] J Gaarder. *Sophie’s World: A Novel About the History of Philosophy*. Farrar, Straus and Giroux, March 2007. ISBN 0374530718.
- [9] A. K. Geim and K. S. Novoselov. The rise of graphene. *Nature materials*, 6(3):183–191, 2007.
- [10] L. M. Ghiringhelli, J. H. Los, A. Fasolino, and E. J. Meijer. Improved long-range reactive bond-order potential for carbon. ii. molecular simulation of liquid carbon. *Phys. Rev. B*, 72: 214103, Dec 2005.
- [11] L.M. Ghiringhelli, C. Valeriani, J.H. Los, E.J. Meijer, A. Fasolino, and D. Frenkel. State-of-the-art models for the phase diagram of carbon and diamond nucleation. *Molecular Physics*, 106(16-18):2011–2038, 2008.
- [12] N. S. Goroff. Mechanism of fullerene formation. *Accounts of chemical research*, 29(2):77–83, 1996.
- [13] J. R. Heath. Synthesis of c60 from small carbon clusters. *Fullerenes*, pages 1–23, 1992.
- [14] L.J. Karssemeijer. Thermal expansion of carbon structures. Master’s thesis, Radboud University Nijmegen, 2010.

- [15] M. I. Katsnelson and A. Fasolino. Graphene as a prototype crystalline membrane. *Accounts of chemical research*, 46(1):97–105, 2012.
- [16] M.I. Katsnelson. Graphene: carbon in two dimensions. *Materials today*, 10(1):20–27, 2007.
- [17] M.I. Katsnelson, K.S. Novoselov, and A.K. Geim. Chiral tunnelling and the klein paradox in graphene. *Nature Physics*, 2(9):620–625, 2006.
- [18] P. Koskinen, S. Malola, and H. Häkkinen. Self-passivating edge reconstructions of graphene. *Phys. Rev. Lett.*, 101:115502, Sep 2008.
- [19] J. Kroes. Graphene nanoribbons and edge reconstructions. Master’s thesis, Radboud University Nijmegen, 2010.
- [20] J. M. H. Kroes, M. A. Akhukov, J. H. Los, N. Pineau, and A. Fasolino. Mechanism and free-energy barrier of the type-57 reconstruction of the zigzag edge of graphene. *Phys. Rev. B*, 83:165411, Apr 2011.
- [21] I.M. Locht. The effect of temperature on the phonon dispersion relation in graphene. Master’s thesis, Radboud University Nijmegen, 2012.
- [22] J. H. Los and A. Fasolino. Intrinsic long-range bond-order potential for carbon: Performance in monte carlo simulations of graphitization. *Phys. Rev. B*, 68:024107, Jul 2003.
- [23] Jan H. Los, Luca M. Ghiringhelli, Evert Jan Meijer, and A. Fasolino. Improved long-range reactive bond-order potential for carbon. i. construction. *Phys. Rev. B*, 72:214102, Dec 2005.
- [24] O. V. Manyuhina. *Frustration in soft matter: interplay between order and curvature*. PhD thesis, Radboud University Nijmegen, 2009.
- [25] A. A. Maradudin, E. W. Montroll, G. H. Weiss, and I. P. Ipatova. *Theory of lattice dynamics in the harmonic approximation*, volume 3. Academic press New York, 1971.
- [26] J. Menendez and J. Page. Vibrational spectroscopy of c60. *Light Scattering in Solids VIII*, pages 27–95, 2000.
- [27] N. Metropolis, A. W. Rosenbluth, M. N. Rosenbluth, A.H. Teller, and E. Teller. Equation of state calculations by fast computing machines. *The journal of chemical physics*, 21:1087, 1953.
- [28] KS Novoselov, AK Geim, SV Morozov, D. Jiang, Y. Zhang, SV Dubonos, IV Grigorieva, and AA Firsov. Electric field effect in atomically thin carbon films. *Science*, 306(5696):666–669, 2004.
- [29] V. Schettino, M. Pagliai, L. Ciabini, and G. Cardini. The vibrational spectrum of fullerene c60. *The Journal of Physical Chemistry A*, 105(50):11192–11196, 2001.
- [30] K. Sellgren, M. W. Werner, J. G. Ingalls, J. D. T. Smith, T. M. Carleton, and C. Joblin. C60 in reflection nebulae. *The Astrophysical Journal Letters*, 722(1):L54, 2010.
- [31] Arkansas Oklahoma Astronomical Society. Astronomers stumble onto huge space molecules. <http://www.aoas.org/article.php?story=20110106144253616>, 2013. (Online; accessed 2 April 2013).

- [32] Nottingham Trent University. Hybridization of carbon. http://www.ntu.ac.uk/cels/molecular_geometry/hybridization/, 2012. (Online; accessed 15 Oktober 2012).
- [33] D. J. Wales, M. A. Miller, and T. R. Walsh. Archetypal energy landscapes. *Nature*, 394(6695):758–760, 1998.
- [34] M. W. Werner, T. L. Roellig, F. J. Low, G. H. Rieke, M. Rieke, W. F. Hoffmann, E. Young, J. R. Houck, B. Brandl, G. G. Fazio, J. L. Hora, R. D. Gehrz, G. Helou, B. T. Soifer, J. Stauffer, J. Keene, P. Eisenhardt, D. Gallagher, T. N. Gautier, W. Irace, C. R. Lawrence, L. Simmons, J. E. Van Cleve, M. Jura, E. L. Wright, and D. P. Cruikshank. The spitzer space telescope mission. *The Astrophysical Journal Supplement Series*, 154(1):1, 2004.
- [35] C.J. Wu, J.N. Glosli, G. Galli, and F.H. Ree. Liquid-liquid phase transition in elemental carbon: A first-principles investigation. *Physical Review Letters*, 89(13):135701, 2002.
- [36] K. V. Zakharchenko, A. Fasolino, J. H. Los, and M. I. Katsnelson. Melting of graphene: from two to one dimension. *Journal of Physics: Condensed Matter*, 23(20):202202, 2011.